FUNDAMENTAL STUDY OF SHEAR CONTROLLABLE SYNTHESIS OF FINE PARTICLES USING TAYLOR-COUETTE FLOW REACTOR

by

LU LIU

A thesis submitted to the University of Nottingham in partial fulfilment of the requirements for the degree of

Doctor of Philosophy

Under the supervision of

Prof. Xiaogang Yang

Dr. Chenggong Sun

JULY 2020

ACKNOWLEGEMENTS

First and foremost, I would like to express my deepest gratitude to my supervisor, Prof. Xiaogang Yang, for his consistent help, physical insight, creative influence and patient guidance throughout my PhD study. Prof. Yang has graciously taken me under his wing these past five years and introduced me to one of his expertise fields - computational fluid dynamics (CFD), leading me to a new world of academic research. It was tough for me at first, but his constructive criticism, immense knowledge and professional guidance helped me to move forward and towards the accomplishment of this work. Prof. Yang's passion and dedication in research has greatly aspired me to be a good researcher after my PhD. In particular, he also generously supported me financially during my thesis pending period. I am very grateful for all that he has offered, including his dedication in reading the final draft of this PhD thesis.

I would like to thank all members in FAST team, Dr. Guang Li, Dr. Jie Yang, Dr. Yiyi Wu, Dr. Luming Chen, Dr. Collins Ezeh, Dr. Bin Dong, Dr. Weibin Shi, Dr. Xiani Huang, Mr. Chenyang Xue, Ms. Yanqing Guo, Ms. Xinyue Cai, Mr. Bin Li, Ms. Shanshan Long and Ms. Lulu Wang for their assistance and meaningful discussions. It has been a great pleasure to work with all of you. I am also glad to have the support of my fellow colleagues, especially Ms. Maxine Yew, Mrs. Dan Wang, Dr. Dongsheng Zhao and Mr. Xiaoping Jiang, the days have never been dull working with you all.

I would especially like to thank my boyfriend, Dr. Xianxu Hou. Thank you for sailing through this journey with me, and always cheering me during the most difficult days. You have been my greatest support and companion. I am also

grateful for my best friends, Ms. Liqun Ma, Ms. Chen Gong, Mrs. Ling Zhao and Mrs. Mengjie Di, for loving me and always being there for me despite the distance.

I would also like to extend my gratitude to the technician team of Faculty of Science and Engineering of the University of Nottingham Ningbo China, Mr. Julian Zhu, Mrs. Helen Xu, Mrs. Jane Zhang, Mrs. Carey Tao, Ms. Kate Yuan, Mr. Jason Wang and Mr. John Zhu, for their technical support in lab experiment.

I would also like to acknowledge the PhD scholarship granted by the International Doctoral Innovation Centre (IDIC) of the University of Nottingham Ningbo China. My sincerest thanks to Ms. Jessica Wang for her administrative support. This work was also financially supported by the National Natural Science Foundation of China (Grant Nos. 21576141, 21606259).

Last but not least, I am indebted to my parents, Mr. Shengping Liu and Mrs. Chuanhong Yang, and my younger siblings Hangchang and Hangmeng for their unconditional love and sacrifices. Thank you for being so understanding and consistently supportive of what I have been pursuing. This would not have been possible without your love.

SYNOPSIS

Fine particles generally have special physicochemical properties, such as good solubility, dispersibility, and adsorption due to their extremely large specific surface area. With such advantages, they have been attracting wide attention in the fields of pharmaceuticals, catalyst, food, cosmetics, chemicals and electronics. Among various methods to prepare fine particle materials, reactive precipitation presents its advantages in terms of simple configuration, flexible operation, and low cost.

Controllable synthesis of fine particles is still a challenge. On one hand, fine particles have a tendency to aggregate or agglomerate due to the relatively reduced effect of gravity force and the enhanced effect of other surface forces, such as van de Waals force. On the other hand, operating conditions, especially the heterogeneity of fluid flow in chemical reactors have complex interaction with particles. Fluid mixing determines the environment for chemical reaction, and fluid shear, especially turbulence induced shear, affects particle growth. Since final material performance depends on particle properties, such as particle size, morphology, porosity, and tap density, it is necessary to investigate the key steps and processes on the course of particle formation in order to realize controllable synthesis and obtain desired products consequently. Thus, this PhD work aims to build the quantitative relationships between the key hydrodynamic parameters involved in the synthesis process using the Taylor-Couette flow (TC) reactor and the synthesised particle properties by employing such reactor. The main work conducted and outcomes derived from the project are summarised as follows:

(1) In chapter 2, barium sulfate was selected as a model substance to study the interfacial phenomenon during the process of particle formation. This chapter is mainly focused on the effect of hydrodynamic process in the TC reactor on particle morphology. Three different kinds of morphology of barium sulfate particles are observed by changing Reynolds number $Re = \frac{\omega d r_i}{\nu}$, feeding rate and supersaturation in the Taylor-Couette flow reactor with a lobed inner cylinder (LTC). Such morphology transition, indicating an interfacial interaction between feed solutions and aggregated particles, is found to be dependent on fluid flow pattern. The mechanism of particle formation under the effect of fluid dynamics is proposed for the LTC.

(2) Following the work of Chapter 2, Chapter 3 is focused on the change of barium sulfate particle size and particle size distribution. The comparison of the particles synthesised using the classical Taylor-Couette flow reactor (CTC) and the LTC reactor was conducted both experimentally and numerically by applying computational fluid dynamics (CFD) modelling. Particles synthesized in the LTC show the overall smaller size with narrower size distribution than those in the CTC, which is also consistent with the CFD modelling results on the effect of shear rate distribution on the particle size distribution. It is suggested that the local turbulence intensification due to geometry modification to the LTC inner cylinder is beneficial to the synthesis of particles with smaller size. Shear induced by small turbulent eddies can have a significant impact on the synthesised particle size.

(3) Chapters 2 and 3 have confirmed that hydrodynamics plays an important role in determining the synthesised particle properties. As the mixing occurring in the TC reactor creates supersaturation, which subsequently induces chemical

reaction, a fundamental study on the mixing was carried out in Chapter 4. Based on the Villermaux iodide-iodate reaction system, the segregation index (*Xs*) was employed as an indicator to evaluate the micromixing efficiency. It is found that the hydrodynamic heterogeneity created by the LTC can significantly enhance the micromixing efficiency. Also, it has been reaffirmed that the micromixing time achieved in the TC reactor is about three orders of magnitude lower than that of the conventional stirred tank reactor. The alteration of the configuration of the inner cylinder can be seen as an effective method to intensify the process of particle preparation.

(4) As the features of Taylor vortices in the TC reactor have been used for particle preparation in this work, the interactions between the vortices embedded with turbulent eddies and the particles were investigated based on tracking the barium sulfate particle trajectories, as discussed in Chapter 5. The simulation reveals that particle motion exhibits a helical movement, entrapped by Taylor vortices. The effective particle diffusion coefficient was introduced in this chapter, which is enhanced by increasing the inner cylinder rotational speed, especially for the LTC, implying that the deformation of Taylor vortices in the gap region of the LTC may significantly affect the entrainment of the particles by such vortices and embedded turbulent eddies. Moreover, particle radial distribution may provide a guidance for particle classification due to the axial velocity gradient, while axial dispersion can be seen as an indicator to characterise the global mixing, which is found to distribute similar to the shape of particle size distribution, indicating the existence of a strong correlation between particle property and particle dispersion due to the turbulence eddies induced shear in the TC reactor. The results from particle tracking simulation

are consistent with the previous studies on the hydrodynamics of the LTC that the use of LTC can intensify the process for particle preparation.

(5) The fundamental study of barium sulfate particle preparation in this PhD project indicates that turbulence eddy induced shear and micromixing occurring in the TC reactor will be beneficial to the realisation of controllable synthesis of fine particle materials. Thus, as an extension of the application, the LTC reactor was also employed for the other reactive system, the co-preparation of $Ni_{0.6}Co_{0.2}Mn_{0.2}(OH)_2$ (NCM622) particles. Both CFD simulation and experimental results clearly show that the synthesized NCM622 particle properties have been improved in the LTC even with a reduced production time of 8 hours, compared to the conventional production method. Reactant mixing was assessed and characterized by two variables using CFD modelling with user-defined scalar (UDS). CFD modelling results show that the effective mixing at both the macro-scale and micro-scale can be quickly achieved in the LTC.

To sum up, this PhD work provides physical insight into the principle of controllable synthesis of fine particle materials. The implication is that the mixing in the TC reactor can create effective supersaturation, thereby inducing reactive precipitation under the effect of hydrodynamic heterogeneity. Such well-established mixing/micromixing environment can be quickly obtained in the TC reactors, especially in the LTC. Meanwhile, the shear induced by various length scale turbulent eddies embedded in the Taylor vortices has a strong correlation with the synthesized particle characteristics. Focuses should be placed on determination of appropriate operation parameters in the actual particle synthesis process when using the TC reactor.

TABLE OF CONTENTS

CHAPTER 2: INTERFACIAL PHENOMENA IN THE SYNTHESIS PROCESS OF BARIUM SULFATE PARTICLES PRECIPITATED IN A LOBED INNER CYLINDER TAYLOR-COUETTE FLOW REACTOR: EFFECTS OF FLUID DYNAMICS

CHAPTER 3: SHEAR CONTROLLABLE SYNTHESIS OF BARIUM SULFATE PARTCLES IN A TAYLOR-COUETTE FLOW REACTOR WITH VARIABLE CONFIGURATIONS OF INNER CYLINDER

CHAPTER 4: EFFECT OF HYDRODYNAMIC HETEROGENEITY ON MICROMIXING INTENSIFICATION IN A TAYLOR-COUETTE FLOW REACTOR WITH VARIABLE CONFIGURATIONS OF INNER CYLINDER

CHAPTER 5: EFFECT OF HYDRODYNAMIC HETEROGENEITY ON PARTICLE AGGREGATE DISPERSION IN A TAYLOR-COUETTE FLOW REACTOR WITH VARIABLE CONFIGURATIONS OF INNER CYLINDER

CHAPTER 6: MODELLING OF TURBULENT SHEAR CONTROLLABLE CO-PRECIPITATION SYNTHESIS OF LITHIUM ION BATTERY CATHODE PRECURSOR MICRO-PARTICLES IN A TAYLOR-COUETTE FLOW

REACTOR WITH VARIABLE CONFIGURATIONS OF INNER CYLINDER

CHAPTER 7: CONCLUSIONS AND RECOMMENDATIONS

LIST OF FIGURES

CHAPTER 1

CHAPTER 2

CHAPTER 3

CHAPTER 4

CHAPTER 5

CHAPTER 6

LIST OF TABLES

CHAPTER 1

CHAPTER 2

CHAPTER 3

CHAPTER 4

CHAPTER 5

CHAPTER 6

NOMENCLATURE

CHAPTER 1

A	embryos surface area, m^2
B	contact nucleation rate, $m^{-3}s^{-1}$
c	molar concentration, mol/L
c_i	molar concentration at crystal-solution interface, mol/L
c^*	molar concentration at equilibrium, mol/L
c_{ie}	species molar concentration in the local environment, mol/L
c_{int}	molar concentration at interface, mol/L
C_B	slab deformation rate constant
C_p	specific heat capacity, J/K/kg
d_m	molecular diameter, m
D_i	molecular diffusion coefficient, m^2/s
D_R	stirred impeller diameter, m
E	engulfment rate, s^{-1}
f	reactor friction factor
g	overall crystal growth rate, m/s
g(t)	volume growing rate in incorporation model
G_c	crystal growth rate, m/s
$\overline{G}$	average shear rate, s^{-1}
ΔG	total molar Gibbs free energy, J/mol
ΔG_v	free energy due to phase change, J/mol
ΔG^*	homogenous nucleation energy barrier, J/mol
ΔG^*_{het}	heterogeneous nucleation energy barrier, J/mol

h	contact nucleation rate exponent
i	contact nucleation rate exponent
j	contact nucleation rate exponent
J_{homo}	homogenous nucleation rate, $m^{-3}s^{-1}$
J_{het}	heterogeneous nucleation rate, $m^{-3}s^{-1}$
k	contact nucleation rate exponent
k_B	Boltzmann's constant, J/K
k_D	mass transfer constant, $m^4/(kmol \cdot s)$
k_d	mass transfer coefficient, m/s
k_g	total growth coefficient, m/s
k_G	overall growth rate constant, m/s
k_n	chemical reaction rate constant
k_R	surface integration constant, $m(dm)^6/(mol^2 \cdot s)$
k_T	thermal conductivity, W/m/K
K	induction time constant
K_N	nucleation rate constant
l_{eddy}	Kolmogorov length scale, m
l_{meso}	meso-mixing length scale, m
L	crystal size, m
L_R	length of reactor, m
M	molecular molar mass, g/mol
M_T	particle mass density, g/m^3
n	kinetic order of nucleation
n	unit normal vector
n_{A0}	initial mole of reactant A
n_{B0}	initial mole of product B
n_{C0}	initial mole of reactant A

n_R	net mole of product R
n_S	net mole of by-product S
n^*	number of molecules forming the critical embryo nuclei
N	stirred frequency, s^{-1}
p	static pressure, Pa
Q	volumetric bulk flow rate, mL/s
Q_{feed}	volumetric flow rate of feeding steam, mL/s
r	nucleus radius, m
r_c	critical nucleus radius, m
r_i	radius of the inner cylinder, m
r_o	radius of the outer cylinder, m
Re	Reynolds number
R_i	chemical reaction rate, $mol/m^3/s$
S	supersaturation ratio/ source term
Sc	Schmidt number
T	thermodynamic temperature, K
Ta	Taylor number
u	fluid velocity in x direction, m/s
u	fluid velocity vector, m/s
$\bar{u}$	fluid local mean velocity, m/s
v	fluid velocity in y direction, m/s
V_e	embryo volume, m^3
V_{ie}	fluid element volume in incorporation model, m^3
V_R	reactor volume, m^3
w	fluid velocity in z direction, m/s
Xs	segregation index
Y	yield of by-product S

Y_{ST}	theoretical yield of by-product S

Greek letters

β	aspect ratio
ε	turbulent energy dissipation rate, m^2/s^3
η	radius ratio
μ	molecular dynamic viscosity, kg/(m·s)
ν	kinematic viscosity of the fluid, m^2/s
ρ	density of the fluid, kg/m^3
ρ_c	crystal density, kg/m^3
σ	surface free energy per unit area, $J/mol/m^2$
τ	shear stress strain rate, $kg/(m \cdot s^2)$
τ_m	characteristic mixing time, s
τ_{macro}	macromixing time, s
τ_{meso}	meso-mixing time, s
τ_{micro}	micromixing time, s
τ_N	nucleation induction time, s
τ_R	characteristic chemical reaction time, s
ω	rotational speed, rad/s
λ	reactor length scale factor, m
Ω	pre-exponential factor for homogenous nucleation
Ω_{het}	pre-exponential factor for heterogeneous nucleation
Φ	generalized variable
Φ_s	slab deformation rate, s^{-1}
Γ	generalized diffusion coefficient, m/s

CHAPTER 2

a	ion activity, mol/kg
A_i	cross sectional area of the inner cylinder, m
B	growth rate, m/s
c	molar concentration, mol/L
Δc	concentration difference, mol/L
d	diameter of particle, m
D	molecular diffusion coefficient, m^2/s
E	engulfment rate, s^{-1}
f	friction factor
G	shear rate, s^{-1}
I	ionic strength, mol/kg
J	nucleation rate, m/s
k_{aggl}	agglomeration rate
K_g	total growth coefficient, m/s
K_{sp}	thermodynamic solubility product, mol^2/L^2
l	length scale, m
l_m	size of agglomerating particle m, m
l_n	size of agglomerating particle n, m
L	reactor length, m
n	kinetic order of nucleation
Pe	Peclet number
Q	feeding rate, mL/min
r_i	equivalent radius of the lobed inner cylinder, m
r_o	radius of the lobed outer cylinder, m
R	gas constant, J/(mol·K)
Re	Reynolds number
R_i	perimeter of the inner cylinder, m

S	saturation ratio
Sa	supersaturation ratio
Sc	Schmidt number
Sh	Sherwood number
St	Stokes number
t_D	diffusion time, s
t_N	induction time, s
t_m	micro-mixing time, s
T	absolute temperature, K
u_t	terminal velocity of particle, m/s
u_θ	azimuthal velocity, m/s
V	volume of reactor, m^3
z	charge number

Greek letters

β_{aggl}	agglomeration efficiency
$\gamma_{\pm}$	activity coefficient
δ_{eq}	equivalent gap, m
Γ	aspect ratio
ε	turbulent energy dissipation rate, m^2/s^2
ζ	angular velocity ratio
η	radius ratio
$\dot{\eta}_V$	volume shear rate, mL/s
λ_{eddy}	eddy length scale, m
μ	viscosity of the fluid, kg/(m·s)
ρ_d	density of particle, kg/m^3
σ	supersaturation

υ	kinematic viscosity of the fluid, m^2/s
φ	molar chemical potential, J/mol
ω_i	rotational speed of the lobed inner cylinder, rad/s

CHAPTER 3

a_i	ion activity of species i, mol/kg
a_{eq}	ion activity at equilibrium state, mol/kg
A_i	cross sectional area of the inner cylinder, m
B	growth rate, m/s
$C_{1\varepsilon}$	model constant for ε equation
$C_{2\varepsilon}$	model constant for ε equation
C_μ	model constant for the calculation of μ_t
d_p	particle size, m
d	gap width, m
D	average crystallite sizes, nm
g	gravity, m/s^2
G	local shear rate, s^{-1}
G_k	generation of turbulence kinetic energy, J
J	nucleation rate, m/s
k	turbulent kinetic energy, m^2/s^2
k_g	growth coefficient, m/s
k_N	nucleation coefficient, m/s
K	shape factor
K_{SP}	thermodynamic solubility product, mol^2/L^2
l_{eddy}	Kolmogorov length scale, m
L	reactor length, m
n	kinetic order of nucleation rate

p	pressure, Pa
Q	volumetric feeding rate, mL/min
r_i	radius of the inner cylinder, m
r_o	radius of the lobed outer cylinder, m
R	correlation coefficient
Re	Reynolds number
R_i	perimeter of the inner cylinder, m
R_ε	extra strain rate, s^{-1}
S	supersaturation ratio
St	Stokes number
t_m	micromixing time, s
t_{res}	average residence time, s
$\mathbf{u}$	fluid velocity, m/s
u_t	terminal velocity, m/s
V	volume of the reactor, mL

Greek letters

β	model constant for the correction of $C_{1\varepsilon}$ term in the ε equation
γ	shear strain rate, s^{-1}
ε	turbulent energy dissipation rate, m^2/s^3
η	model constant for the correction of $C_{1\varepsilon}$ term in the ε equation
η_0	model constant for the correction of $C_{1\varepsilon}$ term in the ε equation
μ	dynamic viscosity, kg/(m·s)
μ_{eff}	effective viscosity, kg/(m·s)
μ_t	turbulent viscosity, kg/(m·s)
ν	kinematic viscosity of the fluid, m^2/s
ρ	density of the fluid, kg/m^3

ρ_p	particle density, kg/m^3
σ_k	turbulent Prandtl number for k equation
σ_ε	turbulent Prandtl number for ε equation
τ	stress tensor, kg/(m·s^2)
ω_i	rotational speed of the inner cylinder, rad/s
δ	peak width, nm
λ	wavelength of X-ray, nm
θ	diffraction angle, rad

CHAPTER 4

A_{353}	absorption at 353 nm
c_j	concentration of species j, mol/L
d	gap width, m
Da	Damköhler number
e_{353}	molar extinction coefficient, L/mol/mm
g	growing rate for incorporation model
I	turbulent intensity, %
I_i	ionic strength, mol/L
k	reaction rate constant, m^2/s^2, dimension dependent on reaction order
K_3	equilibrium constant for Reaction (3)
L	reactor length, m
n_j	mole of species j, mol
r	chemical reaction rate, mol/L/s
r_i	radius of the inner cylinder, m
r_o	radius of the lobed outer cylinder, m
Re	Reynolds number
R_{IXs}	correlation

t_m	micromixing time, s
t_r	chemical reaction time, s
T	thermodynamic temperature, K
Xs	segregation index
Y	yield of iodine

Greek letters

ν	kinematic viscosity of the fluid, m^2/s
ω_i	rotational speed of the inner cylinder, rad/s
Ψ	thickness of quartz cell, mm

CHAPTER 5

C_D	drag coefficient
d_p	particle size, m
$\bar{d}_p$	size constant
d	gap width, m
d_{ij}	deformation tensor
Dz	diffusion coefficient, m^2/s
$\mathbf{F}_{P\text{-}L}$	external force, $kg/(m^2 \cdot s^2)$
g	gravity, m/s^2
k	turbulent kinetic energy, m^2/s^2
L	reactor length, m
$\dot{m}_p$	mass flow rate of particles, kg/s
$\dot{M}_{L-P}$	mass transfer rate, $kg/(m^3 \cdot s)$
n	size spread parameter
N	total number of particles
p	pressure, Pa

r_i	radius of the inner cylinder, m
r_o	radius of the lobed outer cylinder, m
Re	Reynolds number
Re_p	particle Reynolds number
St_η	Stokes number
$\mathbf{u}_L$	instantaneous velocity, m/s
$\overline{\boldsymbol{u}_L}$	Reynolds-average velocity, m/s
$\boldsymbol{u}'_L$	velocity fluctuation, m/s
$\mathbf{u}_P$	particle velocity, m/s
Y_d	accumulated mass fraction of particle
z_i	axial position of the i^{th} particle

Greek letters

ε	turbulent energy dissipation rate, m^2/s^3
ν	kinematic viscosity of the fluid, m^2/s
ρ_L	liquid density, kg/m^3
ρ_p	particle density, kg/m^3
τ_L	stress tensor, $kg/(m \cdot s^2)$
τ_p	particle relaxation time, s
τ_f	characteristic time of flow, s
ω_i	angular velocity, rad/s
Ω	rotational speed of the inner cylinder, rpm
μ	molecular viscosity, $kg/(m \cdot s)$

CHAPTER 6

c_A	concentration of reactant A, mol/L
c_{A0}	initial concentration of reactant A, mol/L

c_B	concentration of reactant B, mol/L
c_{B0}	initial concentration of reactant B, mol/L
$C_{1\varepsilon}$	model constant for ε equation
$C_{2\varepsilon}$	model constant for ε equation
C_μ	model constant for the calculation of μ_t
C_Φ	mechanical-to-timescale ratio
d_p	particle size, m
d	gap width, m
D	average crystallite sizes, nm
g	gravity, m/s^2
$\bar{G}$	local shear rate, s^{-1}
G_k	generation of turbulence kinetic energy, J
k	turbulent kinetic energy, m^2/s^2
K	shape factor
L	reactor length, m
p	pressure, Pa
r_i	radius of the inner cylinder, m
r_o	radius of the lobed outer cylinder, m
R	correlation coefficient
Re	Reynolds number
R_ε	extra strain rate, s^{-1}
Sc_t	turbulent Schmidt number
St_η	Stokes number
t_Φ	micromixing time, s
u	Reynolds-average velocity, m/s

Greek letters

γ	micromixing rate, s^{-1}
ε	turbulent energy dissipation rate, m^2/s^3
μ_{eff}	effective viscosity, kg/(m·s)
ν	kinematic viscosity of the fluid, m^2/s
ρ	density of the fluid, kg/m^3
ρ_p	particle density, kg/m^3
σ_k	turbulent Prandtl number for k equation
σ_ε	turbulent Prandtl number for ε equation
$\boldsymbol{\tau}$	stress tensor, $kg/(m \cdot s^2)$
τ_p	particle relaxation time, s
τ_f	characteristic time of fluid flow, s
$\bar{\xi}$	mean mixture fraction
$\overline{\xi'^2}$	mean mixture fraction variance
ω_i	rotational speed of the inner cylinder, rad/s
δ	peak width, nm
λ	wavelength of X-ray, nm
θ	diffraction angle, rad
Γ_T	turbulent diffusivity, m/s
η	Kolmogorov length scale, m

CHAPTER 6

MODELLING OF TURBULENT SHEAR CONTROLLABLE CO-PRECIPITATION SYNTHESIS OF LITHIUM ION BATTERY CATHODE PRECURSOR MICRO-PARTICLES IN A TAYLOR-COUETTE FLOW REACTOR WITH VARIABLE CONFIGURATIONS OF INNER CYLINDER

SUMMARY

From previous fundamental study of barium sulfate particles synthesized in the TC reactor, it is found that such device is promising in terms of process intensification and particle property control, thereby having wide applications to the preparation of various particles. Firstly, the relatively homogenous hydrodynamic condition in such TC reactor system is favourable for the formation of spherical particles. Different from traditional reactors, the vortices are evenly distributed along the axial direction in the TC reactor with the same length scale. Accordingly, turbulence induced eddies down to the particle length scale are recognised to be isotropic. Thus, eddy shear can evenly act on particle surface, facilitating particles to become spherical. Secondly, the scale of these turbulent eddies can be easily controlled by adjusting operating parameters, such as rotational speed, and axial velocity. Accordingly, the eddy capacity to load particles can be adjusted. As agglomeration of primary particles results in the formation of secondary particles, which takes place within eddies, eddies can be suggested to play a critical role in determining final particle compactness.

Based on the observation of barium sulfate particle preparation and the aforementioned reasons, controllable synthesis of particles can be realized in the TC reactor. Therefore, as an extension, TC reactor was also applied to the other reactive synthesis system, the preparation of $Ni_{0.6}Co_{0.2}Mn_{0.2}(OH)_2$ (NCM622) particles, using both CFD simulation and experimental validation. There are two main reasons for the choice of such particles. Firstly, lithium ion batteries have attracted many attentions in recent years due to their wide applications to electronic equipment and hybrid electronic vehicles. As one of the most promising cathode precursor materials, NCM622 has the potential to be commercialized. As the TC reactor used in this work can be scaled up into industrial application, the product properties can be easily compared with the commercially used materials. Secondly, after a careful review of previous studies, it is found that these studies mainly focused the optimization of chemical factors, but failed to realize the controllable particle synthesis to obtain regular shape. However, spherical particles are preferred among various morphologies. They often have high tap density, which is beneficial for the improvement of electrochemical performance. As confirmed in previous chapters, the turbulent eddied generated in the TC reactor are beneficial for the formation of compact agglomerates and regular spherical shape. Therefore, considering the above factors, NCM622 was chosen as a target object and the TC reactor is suitable for such reactive system. The experimental co-precipitation in the CTC and LTC focused on the effects of processing time and local turbulent shear rate. CFD simulation was employed to reveal the difference of flow field at various operating conditions. Both CFD simulation and experimental results show that the increased shear rate can lead to the decrease of the final synthesised micro-particle size due to the suppression of particle growth by turbulence eddy induced shear. Taylor-Couette flow by using

the lobed inner cylinder can achieve an enhanced shear rate in the impinging jet regions formed in the vicinity of the inner cylinder surface due to the occurrence of a large radial velocity gradient. Consequently, the synthesised micro-particle properties such as morphology and specific surface area in the LTC are much more improved than those in the CTC. The mixing was also assessed and characterised by two variables, mean mixture fraction and its variance, predicted by use of CFD modelling with user-defined scalar (UDS), and correlating with the effect of shear rate for both the CTC and LTC. CFD simulation reveals that effective mixing at both the macro-scale and micro-scale can be quickly achieved in the LTC.

6.1 Introduction

Lithium ion batteries have commonly been recognised and widely employed as the most effective electric energy storage source and has received significant attention from various applications (Ren *et al.*, 2017). In order to manufacture the lithium ion batteries, the most commonly used transition metal elements for cathode materials are nickel, cobalt and manganese. However, $LiNiO_2$ is difficult to synthesise and has a poor thermal stability (Morales *et al.*, 1990). It has also been found that layered $LiMnO_2$ can easily be transformed into a spinel structure during charging and discharging processes. The spinel structure has a major drawback of the capacity fading due to the lattice distortion of manganese (Ceder and Mishra, 1999). On the other hand, many previous studies have indicated that $LiCoO_2$ can offer many advantages, such as high rate capability and excellent cycling performance, but its toxicity and high cost confines its application in industrial production (Liang *et al.*, 2014). Thus, some previous

studies have focused on developing new cathode materials for lithium ion batteries, such as the partial replacement of single transition metal, or the development of new modification approaches, such as coating and doping (Kweon *et al.*, 2000; Kim *et al.*, 2006; and He *et al.*, 2012).

The layer ternary material $LiNi_xCo_yMn_{(1-x-y)}O_2$ series combines the advantages of $LiNiO_2$, $LiCoO_2$ and $LiMnO_2$, and demonstrates relatively high capacity, thermal stability and good cycling performance (Liang *et al.*, 2014). Among this series of materials, $LiNi_{1/3}Co_{1/3}Mn_{1/3}O_2$ has been commercially used. However, its low capacity (150-160 mAh/g) requires improvement (Lee *et al.*, 2004). Ni-rich cathode materials are promising candidates due to their relatively high capacity and low cost, which can reach a capacity of up to 220 mAh/g with an average value of 170 mAh/g (Liang *et al.*, 2014; and Yang *et al.*, 2016). Among these Ni-rich cathode materials, $LiNi_{0.6}Co_{0.2}Mn_{0.2}O_2$ (LiNCM622) has shown its considerable capacity at a low cut-off voltage range (< 4.3 V) and low cost with a rather low content of cobalt (Yuan *et al.*, 2017). Cao *et al.* (2005) have obtained LiNCM622 with an initial discharge capacity of 175.3 mAh/g, which still manages to retain the capacity of more than 150 mAh/g even after 70 cycles. Sun *et al.* (2016) synthesised LiNCM622 at a high calcination temperature, and the material has shown a good low-temperature property (157 mAh/g at 0 ℃). Chen *et al.* (2018) have successfully prepared concentration-gradient LiNCM622 via the co-precipitation method. The cathode material that they have synthesised has shown an excellent initial discharge capacity of up to 195.6 mAh/g with a capacity retention of about 90% after 100 cycles. All these studies have clearly demonstrated the importance of the synthesis process.

In order to obtain the final LiNCM622 cathode material, the first step is to synthesise the hydroxide precursor of $Ni_{0.6}Co_{0.2}Mn_{0.2}(OH)_2$ (NCM622), followed by calcination with LiOH or Li_2CO_3. It has been suggested that LiNCM622 can inherit the morphology and structure from NCM622 precursor (Liang *et al.*, 2014; Cheng *et al.*, 2017; and Yuan *et al.*, 2017), which means that the property of the final cathode material is dependent on the formation of the NCM622 precursor. Therefore, it is necessary to investigate the key operation parameters that are adopted in the reactors during the synthesis process of NCM622 precursor. Various synthesis methods have also been trialled and employed, such as spray-drying (Yue *et al.*, 2011), solid-state method (Gan *et al.*, 2005), sol-gel method (Lee *et al.*, 2016). Most of these methods are intermittent with low productive efficiency, which is not beneficial to commercial and industrial applications. Compared to the aforementioned methods, co-precipitation is more efficient as it can be operated continuously, which is much more beneficial to large-scale production in industry. Also, the use of co-precipitation can achieve a relatively homogenous distribution of these three metals (Lee *et al.*, 2004). Although a large amount of research work has been done, previous work has mainly focused on the impacts of factors such as the pH value of the solution, ammonia concentration and reactive environmental temperature (Cao *et al.*, 2005; Liang *et al.*, 2014; and Ren *et al.*, 2017). Furthermore, the majority of the synthesis processes were conducted in the traditional stirring tank, resulting in a long processing time of at least 60 hours (Cui *et al.*, 2019) and irregular shapes of NCM622 micro-particles.

Recent studies on the synthesis of micro-particles by precipitation have indicated that the hydrodynamics in the precipitation has a significant impact on the final particle size and morphology. Ren *et al.* (2017) used a stirred tank

with the impeller of double blades to prepare the NCM622 precursor, and they obtained spherical secondary particles, formed from closely packed primary particles at 1000 rpm. In Liang *et al.*'s (2014) study, the effect of stirring speed was explored and it was observed that spherical particles exhibit a smooth surface and a high tap-density of 1.91 g/cm^3 at 800 rpm. These studies have implicitly indicated that the synthesis of particles is very likely correlated with the local hydrodynamics involved, especially the local turbulence status. It should be also noted that these studies were only concerned with one hydrodynamic parameter, the stirring rate. Although the use of stirring speed can approximately expose the macro hydrodynamic environment for the formation of the particle suspension, it is still not able to reveal the relationship between the formation of the particles and the local hydrodynamics, which is suggested to be characterized by the local turbulence behaviour or turbulent shear. Zhu *et al.* (2019) have studied the utilisation of four different types of impeller to synthesise the NCM622 precursor. As a result, they suggested that the impeller may determine the hydrodynamics experienced by particle formation, affecting nuclei formation and the growth of primary particles. Their explanation on the mechanism involved in the synthesis lacks the support of theoretical analysis or CFD simulation of the flow taking place in the stirred tank. In addition, they have adopted a long processing time of at least 50 hours in their experiments in order to obtain regular spherical particles when using the traditional stirred tank reactor. The correlation between the processing time and the synthesised particle properties was not revealed.

The use of other types of reactor to prepare micro-fine particles was also reported in the literature. Typical examples are the T-mixer (Gradl *et al.*, 2006), impinging jet reactor (Casanova and Higuita, 2011), vortex mixer (Bensaid *et*

al., 2014) and TC reactor (Thai *et al.*, 2015). The common feature of these reactors is the enhancement and intensification of the local turbulence for the purpose of increasing the local turbulence induced shear. Among all these reactors, the TC reactor can be regarded as a promising device as it can provide controllable flow patterns and a narrow shear rate distribution (Li *et al.*, 2015). To the best of our knowledge, only a few studies have reported the adoption of the TC reactor to synthesise the NCM622 precursor, but with the traditional rotational circular inner cylinder. The effect of the micromixing in such a reactor on the synthesised NCM622 particle properties is still not clear and requires further investigation. As numerous previous studies have investigated the effects of reactive parameters including pH value, ammonia concentration and reactive environmental temperature on particle synthesis process (Cao *et al.*, 2005; Liang *et al.*, 2014; and Ren *et al.*, 2017), this study particularly focuses on the hydrodynamics in the synthesis of particles using the TC reactors, highlighting the effect of local turbulent shear rate on the formation and growth of particles. Also, the modelling of reactant mixing in the TC reactor but with two different inner cylinders, traditional circular inner cylinder and lobed inner cylinder is concerned. We aim to reveal how the use of different inner cylinders with cross-section profiles affect the mixing, including the correlation between the local turbulent induced shear and local micromixing. As turbulent flow in such a reactor is still not easily obtained from experimental measurement such as the use of PIV and LDV, a CFD modelling approach has been adopted in this study, coupling the mixing evaluation as suggested by Marchisio *et al.* (2006).

This chapter will be organised as follows. Section 6.2 will present the experimental details for co-precipitation of NCM622 precursor particles and characterisation while Section 6.3 will present the CFD modelling on the

synthesis in the TC reactor with micromixing mathematical modelling. Section 6.4 will present the numerical simulation results and discussion, focusing on the formation of synthesised particles and the correlation between the micromixing, and local turbulent shear. Section 6.5 will summarise the conclusions derived from the study.

6.2 Experimental

6.2.1 Apparatus setup

The apparatus of the TC reactor for the synthesis of $Ni_{0.6}Co_{0.2}Mn_{0.2}(OH)_2$ (NCM622) precursor particles is schematically shown in Figure 6.1 (a). This particular setup consists of two cylinders with the inner cylinder rotating and the outer cylinder being static in the working mode. In order to reduce the effect of hydrostatic pressure, the reactor was placed horizontally, where the inlets and outlet were installed at the same level along the axial direction. Also, it was observed from the preparation of $BaSO_4$ particles in previous chapters that some gas bubbles may appear when feeding reactant solutions. Due to the buoyancy force, these bubbles will go throughout the whole reactor, leading to a perturbation, and unstable product properties. Additionally, under the effect of fluid gravity, Taylor vortex will be extruded, thus losing its original shape at the bottom of the reactor. The longer the reactor length, the more significant the shape changes. Thus, for a more precisely operation, TC reactor was located horizontally in NCM622 synthesis. Two types of inner cylinder that were adopted in the present study. One is the classical inner cylinder with a circular cross-sectional profile while the other is a lobed inner cylinder as shown in Figure 6.1 (b). Herewith, we use the abbreviations of CTC and LTC to denote

the classical TC reactor and the lobed TC reactor, respectively. The dimensions of both types of reactor are described in Table 6.1.

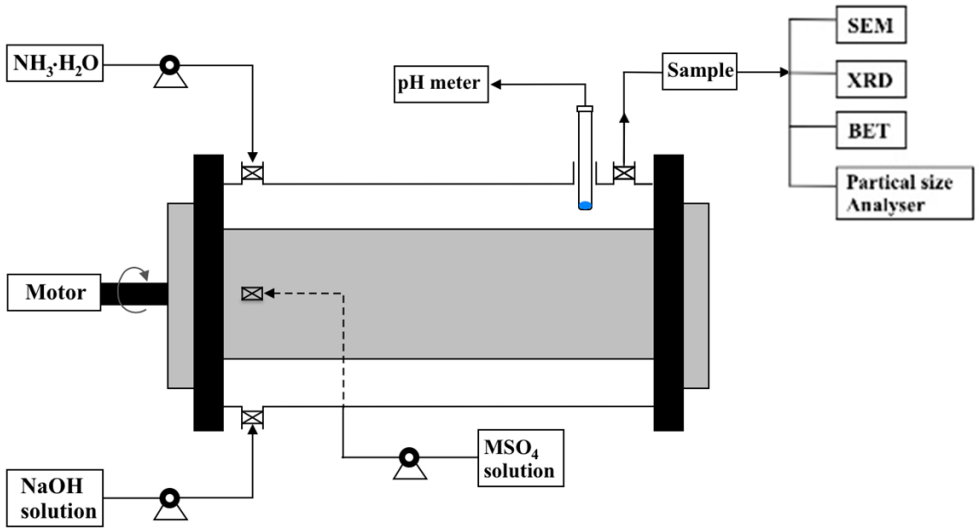

(a)

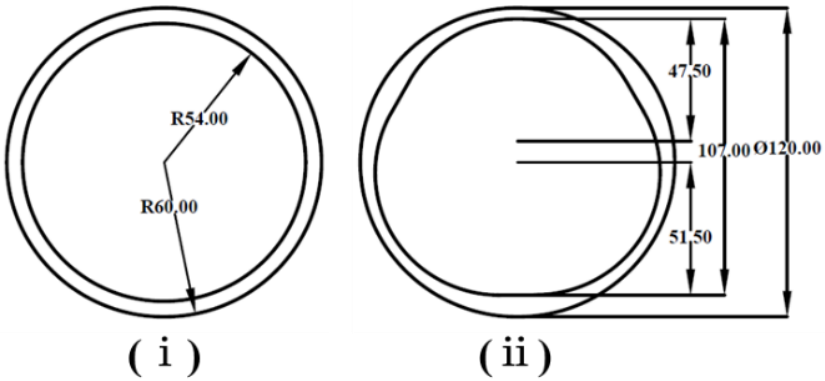

(b)

Figure 6.1 (a) Schematic diagram of experimental apparatus; and (b) Schematic of cross-section profiles for the: (i) CTC; and (ii) LTC.

Table 6.1 Dimensions of the TC reactor.

Dimension	CTC	LTC
Reactor length, L (mm)	160.00	160.00
Outer cylinder radius, r_o (mm)	60.00	60.00
Inner cylinder radius, r_i (mm)	54.00	53.80
Gap size, d (mm)	6.00	6.20

6.2.2 Co-precipitation synthesis of NCM622

The agents, nickel sulfate hexa-hydrate ($NiSO_4 \cdot 6H_2O$, analytical grade), cobalt sulfate hepta-hydrate ($CoSO_4 \cdot 7H_2O$, analytical grade) and manganese sulfate monohydrate ($MnSO_4 \cdot H_2O$, analytical grade) were chosen for the preparation of reactant solution. The molar ratio of the three mental ions (Ni:Co:Mn) was kept at 0.6:0.2:0.2 to form 2.0 mol/L sulfate (MSO_4) solution. A 4.0 mol/L sodium hydroxide (NaOH, analytical grade) solution was used as the precipitator. Ammonia ($NH_3 \cdot H_2O$, analytical grade) was supplied as the complexing agent, and the molar ratio of $NH_3 \cdot H_2O$ to MSO_4 was kept at 1.0. In the present work, all gaents were purchased from Sinopharm Chemical Reagent Co., Ltd.

As pH is a critical factor in determining final product quality, a trial has been conducted preliminarily in identifying the appropriate pH value. Figure 6.2 (a) shows the colour change of upper liquid at the pH value of 11.3, 11.6, and 11.9. For a low pH value, the upper liquid is blue, which indicates too much ammonia complexation of metal ions formed rather than the metal hydroxide (Liang *et al.*, 2014). While, too high pH value will facilitate the formation of manganese oxide rather than manganese hydroxide, which makes the upper liquid brown (Lee *et al*., 2004; and Liang *et al.*, 2014). Also, the SEM images in Figure 6.2

(b) indicates that at too low or too high pH value is not beneficial to form an irregular spherical NCM622 particles. At the pH value of 11.3, particles shows various morphologies with non-uniform size due to the random agglomeration of secondary particles. When pH value reaches 11.9, primary particles are assembled very loosely to form secondary particles without smooth surface.

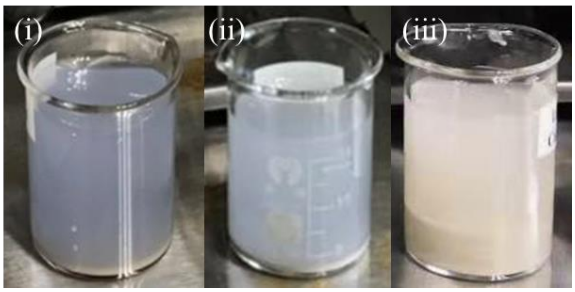

(a)

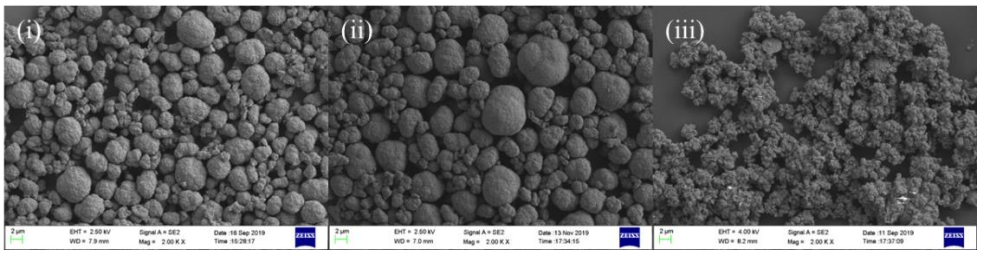

(b)

Figure 6.2 (a) Product suspension colour; and (b) Product morphology at different pH values: (i) 11.3; (b) 11.6; and (c) 11.9.

The TC reactor was firstly filled with deionized water to remove air. The reactor was then heated to 55 ℃ and maintained at this particular temperature by using a heating jacket. A little amount of $NH_3 \cdot H_2O$ was pumped into the reactor at the base, followed by the synchronous feeding of MSO_4 solution and NaOH solution from individual inlets. Based on the volume of TC reactor, the total feeding rate contributed from the three inlets were adjusted to fix a mean

residence time of 1 hour, where the feeding rates of MSO_4 solution and NaOH solution were equal, and the feeding rate of ammonia was 1/3 of each reactant feeding rate. Meanwhile, during the co-precipitation process, the feeding rate of NaOH solution was adjusted slightly to maintain the pH value at 11.6±0.05. As $NH_3 \cdot H_2O$ serves as complex agent to provide NH_3, firstly combining metal ions, the mechanism of the formation of NCM622 crystals can be expressed by two-step process.

$$0.6Ni^{2+} + 0.2Co^{2+} + 0.2Mn^{2+} + nNH_3 \cdot H_2O \rightarrow [Ni_{0.6}Co_{0.2}Mn_{0.2}(NH_3)_n]^{2+} + nH_2O$$

$$[Ni_{0.6}Co_{0.2}Mn_{0.2}(NH_3)_n]^{2+} + 2OH^- + nH_2O \rightarrow Ni_{0.6}Co_{0.2}Mn_{0.2}(OH)_2 + nNH_3 \cdot H_2O$$

This co-precipitation was operated in a continuous mode, which ensures the reactants were continuously fed from inlets, and the synthesised micro-particle suspensions were continuously collected from the outlet. The key parameters are the processing time and the rotational speed of the inner cylinder in the CTC and LTC. After a given time period, the collected samples were washed with deionized water until the rinsed water was found to be neutral. Following this step, the suspension samples were then filtered and the filter cakes were dried at 80 ℃ for 24 h in the oven to obtain NCM622 precursor particles.

6.2.3 Characterisation

Particle size distribution of the synthesised NCM622 particles were determined by Malvern Mastersizer (Bettersize 2000, China). The corresponding morphology was observed using SEM (Sigma VP, ZEISS, Germany), coupled

with the confirmation of elemental composition by using energy dispersive X-ray spectroscopy (EDX). The mass ratio of the three metal elements was measured by inductively coupled plasma optical emission spectroscopy (ICP-OES, SPECTRO ARCOS, Germany). Pore size and the specific area were measured using BET (Micromeritics ASAP 2020, U.S.A). The crystallite structure was analysed using XRD with Cu-Kα radiation source (λ=1.54056 Å) (Bruker-AXS D8 advance powder diffractometer, Germany).

6.3 CFD modelling

6.3.1 Governing equations

The use of Reynolds number to describe the flow pattern in TC reactor has been suggested by many previous studies (Lathrop *et al.*, 1992; and Grossmann *et al.*, 2016), which is defined by

$$Re = \frac{\omega_i r_i d}{\nu} \tag{6.1}$$

where ω_i and r_i are the angular velocity and the radius of the inner cylinder, respectively, d is the gap size, and ν is the kinematic viscosity. The critical Reynolds number (Re_c) serves as an indicator of the appearance of Taylor vortex flow. With the increase of angular velocity, the flow will undergo a series of instabilities until it develops into turbulent Taylor flow (Lathtop *et al.*, 1992). For the current study, the minimum rotational speed was set at 300 rpm, corresponding to a Reynolds number of 3728, which is far greater than the critical Reynolds number, Re_c=1728. Therefore, the flow in the reactor can be judged as turbulent flow. The turbulent flow field in the TC reactor was

simulated with the Reynolds Average Navier-Stokes equations (RANS) coupled with RNG k-ε model to close the equations. The governing equations for continuity and momentum, and the RNG k-ε model are given as follows,

Continuity equation:

$$\nabla \cdot \boldsymbol{u} = 0 \tag{6.2}$$

Momentum conservation equation:

$$\frac{\partial}{\partial t}(\rho \boldsymbol{u}) + \nabla \cdot (\rho \boldsymbol{u}\boldsymbol{u}) = -\nabla p + \nabla \cdot \boldsymbol{\tau} + \rho \boldsymbol{g} \tag{6.3}$$

k equation:

$$\frac{\partial}{\partial t}(\rho k) + \nabla \cdot (\rho k \boldsymbol{u}) = \nabla \cdot \left(\frac{\mu_{eff}}{\sigma_k} \nabla k\right) + G_k - \rho \varepsilon \tag{6.4}$$

ε equation:

$$\frac{\partial}{\partial t}(\rho \varepsilon) + \nabla \cdot (\rho \varepsilon \boldsymbol{u}) = \nabla \cdot \left(\frac{\mu_{eff}}{\sigma_\varepsilon} \nabla \varepsilon\right) + C_{1\varepsilon} \frac{\varepsilon}{k} G_k - C_{2\varepsilon} \rho \frac{\varepsilon^2}{k} - R_\varepsilon \tag{6.5}$$

where $\boldsymbol{u}$ is the Reynolds-average velocity, ρ is the fluid density, p is the static pressure, $\boldsymbol{\tau}$ is the stress tensor, $\boldsymbol{g}$ is the gravity. For k and ε equations, k is the turbulent kinetic energy, ε is the turbulent energy dissipation rate, μ_{eff} is the effective viscosity, σ_k and σ_ε are turbulent Prandtl numbers, G_k is the generation of turbulent kinetic energy, $C_{1\varepsilon}$ and $C_{2\varepsilon}$ are model constants, and R_ε is the extra

strain rate (Yakhot *et al.*, 1992). The details of flow field simulation refer to our previous study (Liu *et al.*, 2020).

6.3.2 Mixing model for co-precipitation synthesis

The mixing performance in the TC reactor that brings two separate flow streams of reactant (MSO_4 solution complexed with ammonia; NaOH solution) into contact to obtain NCM622 suspension particles can be evaluated by using the micromixing model, proposed by Fox (2003). The mixing efficiency can be described by a non-reacting scalar, mixture fraction ξ. For a non-premixed reaction system, (A+B→P), the mixture fraction is a conserved scalar, which is related to the local concentration of reactants A and B, defined by

$$\xi = \frac{c_A - c_B + c_{B_0}}{c_{A_0} + c_{B_0}} \tag{6.6}$$

where c_{A_0} and c_A are the initial concentration and the local concentration of reactant A, c_{B_0} and c_B are the initial concentration and the local concentration of reactant B. By definition, the value of mixture fraction will fall into the range between 0 and 1, indicating the degree of local mixing under the influence of turbulent shear flow condition for CFD modelling. The Reynolds-average transport equation to describe such scalar can be written as (Fox, 2003),

$$\frac{\partial \rho \bar{\xi}}{\partial t} + \nabla \cdot (\rho \boldsymbol{u} \bar{\xi}) = \nabla \cdot (\rho \Gamma_T \nabla \bar{\xi}) \tag{6.7}$$

where Γ_T is the turbulent diffusivity. It can be calculated using the turbulent Schmidt number and Boussinesq hypothesis by the following equation,

$$\Gamma_T = \frac{C_\mu}{Sc_t}\frac{k^2}{\varepsilon} \tag{6.8}$$

where C_μ is a constant equal to 0.09, and the turbulent Schmidt number Sc_t takes a value of 0.7. However, the mean mixture fraction is unable to describe the actual turbulent scalar fluctuations. This information is suggested to be provided by another variable, mixture fraction variance $\overline{\xi'^2}$ (Liu and Fox, 2006; Marchisio *et al.*, 2006; and Duan *et al.*, 2016). Theoretically, for a perfect mixing region, the value of $\overline{\xi'^2}$ should be zero due to no segregation existence. The Reynolds-average transport equation for $\overline{\xi'^2}$is given as follows,

$$\frac{\partial \rho \overline{\xi'^2}}{\partial t} + \nabla \cdot (\rho \boldsymbol{u} \overline{\xi'^2}) = \nabla \cdot (\rho \Gamma_T \nabla \overline{\xi'^2}) + 2\rho\Gamma_T |\nabla \bar{\xi}|^2 - 2\rho\gamma\overline{\xi'^2} \tag{6.9}$$

The second term on the right hand is the production term, which is generated by the gradients of the mean mixture fraction. The last term is the dissipation term due to micromixing. In order to solve the equation, a closure for this term is necessary. The micromixing parameter γ is modelled using the following approximation (Fox, 2003),

$$\gamma = \frac{C_\Phi}{2}\frac{\varepsilon}{k} \tag{6.10}$$

where γ is defined as the micromixing rate. C_Φ denotes the mechanical-to-timescale ratio (Bensaid *et al.*, 2014) and is a function of local Reynolds number of the turbulent eddies with the Schmidt number larger than 1000. For a fully turbulent flow, C_Φ is found to be around 2.0. In addition, the characteristic decay time t_Φ for sub-scale segregation can be estimated according to Equation (6.11),

$$t_{\Phi} = \frac{1}{2\gamma} \tag{6.11}$$

where t_{Φ} can be further interpreted as the local micromixing time, which is the time required to destroy micro-scale gradient within sub-grid scale to achieve complete mixing at molecular level.

6.3.3 Numerical modelling

CFD modelling of the turbulent vortex flow in the TC reactor was conducted using commercial software, Fluent 17.0. The computation domain was set up with the Design Modeller while the computational mesh was created using ANSYS ICEM. For modelling of the flow in the LTC, a sliding mesh was adopted in the vicinity of the inner cylinder due to the lobed cross-section profile. The gap region between the inner cylinder and the outer cylinder was divided into two zones, where the inner one contained the lobed inner cylinder, whose rotational speed was set by mesh motion. The total meshes of the computational domain have around 400000 cells. As the mesh size in the radial direction is crucial for identification of the detailed structure of Taylor vortices and the local velocity gradient, the trial simulation on mesh independence check was conducted by only changing the node number along the radial direction with the meshes of 10×180×160, 14×180×160, and 24×180×160 (radial×circumferential×axial). The trial simulation results have shown that the differences between the two setups of 14×180×160 and 24×180×160 are marginal, indicating that the former mesh adopted has been fine enough to ensure numerical accuracy. The mesh 14×180×160 has thus been adopted in the numerical modelling of the turbulent flow and micromixing in the TC reactor.

The boundary conditions at inlets and outlet were set as velocity inlet and pressure outlet, respectively. The convergence criteria for the simulation was set at 1.0×10^{-3}, and the time step size was set at 10^{-4} s for temporal discretisation. The QUICK scheme has been applied for the spatial discretisation of the convective terms, and the pressure-velocity coupling was realised by the SIMPLEC algorithm.

The micromixing model was implemented by the user defined scalar (UDS) into FLUENT to predict the mixing performance of the reactants, where the mean mixture fraction $\bar{\xi}$ and the mixture fraction variance $\overline{\xi'^2}$ were solved using Equations (6.7) and (6.9) with $X_1 = \bar{\xi}$, and $X_2 = \overline{\xi'^2}$. The initial boundary conditions at the inlet for the MSO_4 solution were $X_1 = 1.0$, and $X_2 = 0.0$, and for NaOH solution were $X_1 = 0.0$, and $X_2 = 0.0$. Since the solution density and viscosity are constant, the flow field in the reactor can be calculated firstly, independent of other scalars' transport equations. The scalars of micromixing model were solved with the first order upwind scheme after the turbulent vortex flow field was obtained. The convergence criteria of both scalars were set at 1×10^{-4}.

6.4 Results and discussion

6.4.1 Effects of processing time and the local turbulence induced eddies in the TC reactor on the synthesised particle properties

The co-precipitation reaction was driven by local supersaturation, generated from the contact of the feeding solutions. Generally, for a continuous feeding mode, a time period is necessary for the products to reach a steady state. In the

current study, the processing time is defined as the time elapsed from the reaction startup to the end of sample collection. In order to determine such a time period, the collection of the synthesised NCM622 particles were continuously trialled from the reactor outlet for a specified time interval, which is equal to the mean residence time (i.e., 1 h). The processing time ranges from 1 hour to 8 hours.

Figure 6.3 (a) shows the evaluation of particle morphology with processing time at a mean shear rate of 1604 s^{-1} , calculated by using Equation (6.16) and corresponds to an inner cylinder of rotational speed at 1100 rpm, and the Reynolds number of 13668 in the CTC. From the SEM images, it can be seen clearly that the final NCM622 particles are the secondary particles, assembled by the very thin sheet-like primary particles. These secondary particles were formed as the result of agglomeration. At the onset of the reaction, the initial form of primary particle is crystallite.

In addition, the composition of the synthesised particles were identified by EDX. Figure 6.3 (c) shows the elemental distribution of Ni, Co and Mn respectively at a processing time of 8 hours. The individual images and the merged image indicate a homogenous distribution of these three metals. In order to further ensure the components are properly presented in final NCM622 particles, the mass ratio of nickel, cobalt and manganese were measured and then converted into molar ratio, shown in Table 6.2. It can be seen that there is no significant difference in terms of molar concentration of three major elements between the processing time at 7 hours and 8 hours. Also, the molar ratio is near to the prescribed ratio of 0.6:0.2:0.2. This result indicates that the proper NCM622 precursor particles can be synthesized within a short processing time by using

the TC reactor. Thus, the TC reactor is suggested to be a promising device to increase productivity.

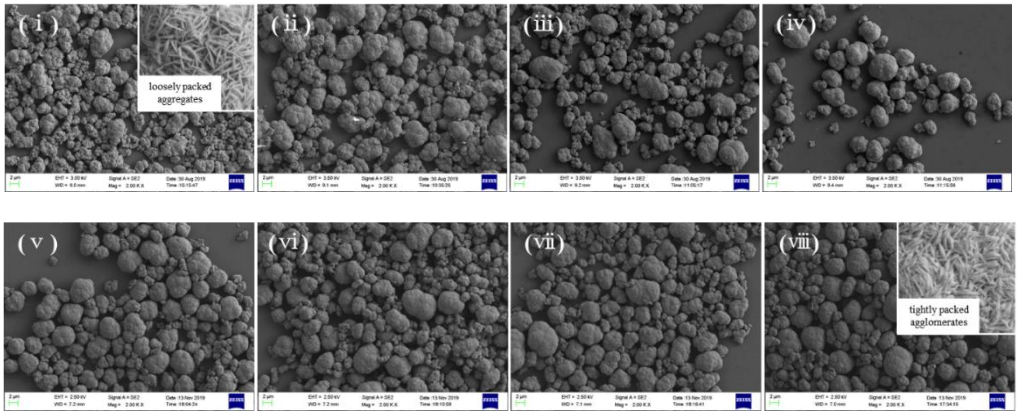

(a)

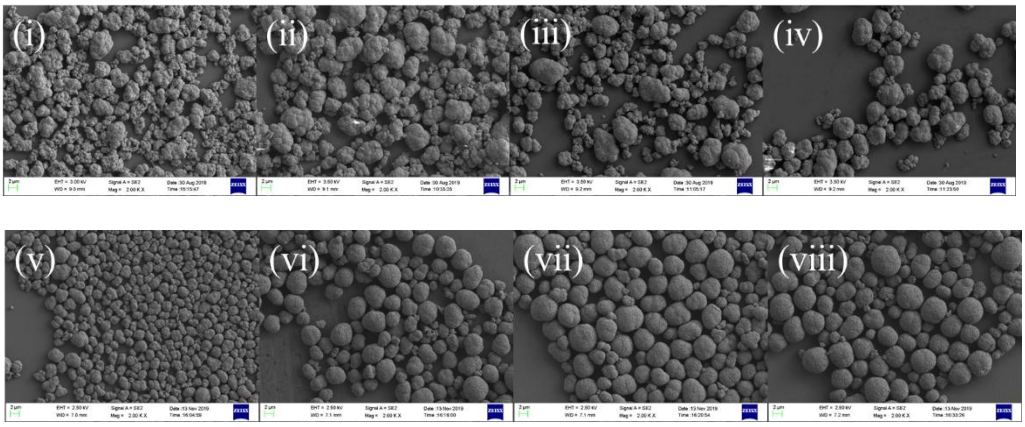

(b)

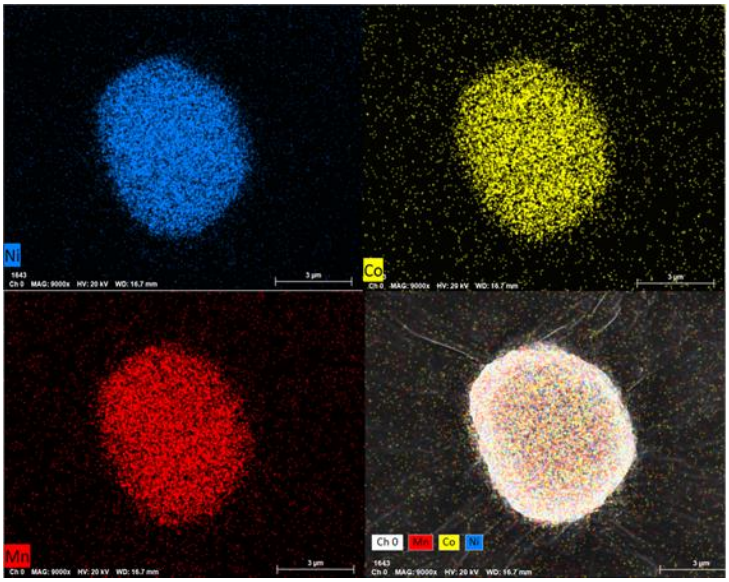

(c)

Figure 6.3 (a) SEM images of NCM622 in the CTC; and (b) LTC at different processing times: (i) 1 h; (ii) 2 h; (iii) 3 h; (iv) 4 h; (v) 5 h; (vi) 6 h; (vii) 7 h; and (viii) 8 h; and (c) elemental mapping at a processing time of 8 hours.

Table 6.2 Element concentration.

Processing time (hours)	Mass ratio wt%			Molar ratio		
	Ni	Co	Mn	Ni	Co	Mn
7	39.4	14.1	12.6	0.59	0.21	0.20
8	39.8	13.9	12.4	0.59	0.21	0.20

The XRD pattern in Figure 6.4 shows the crystal structure of NCM622, which is similar to the crystal structure of β-$Ni(OH)_2$. All diffraction peaks present a typical hexagonal structure with a space group of $P\bar{3}m1$. The result indicates that Mn^{2+} and Co^{2+} entered the internal lattice structure of $Ni(OH)_2$, substituting

some Ni^{2+} (Lee *et al.*, 2004; Thai *et al.*, 2015; and Xu *et al.*, 2018). This is the reason for the absence of the diffraction peaks of $Mn(OH)_2$ and $Co(OH)_2$ as shown in Figure 6.4. The high intensity of plane (001), plane (100), and plane (101) reveals the orientation of crystal growth (Thai *et al.*, 2015). Moreover, the relatively broader full width at the half maximum height (FWHM) of plane (001) indicates a smaller crystallite size, calculated using the Scherrer equation, given by Equation (6.15). Furthermore, it can be deduced from the different sizes of the three typical planes that planes (001) and (101) are thinner, while plane (100) is longer, which indicates a plate-like primary particles synthesised initially. It can be postulated that due to highly intensive turbulent eddy fluctuation, the existing primary particles trapped by small eddies may collide with each other. This collision can lead to the formation of the loosely packed aggregates (marked in Figure 6.3 (a)), which will be transported and re-dispersed under the influence of various size turbulent eddies. Figure 6.5 illustrates the radial velocity field in the vertical cutting plane. It can be seen that Taylor vortices are present in terms of a pair of counter-rotating toroidal vortices, highlighted in Figure 6.5. There exists either radially inward or outward impinging jet regions between Taylor vortex pairs. The local large velocity gradient generated in the impinging jet regions results in the high shear rate. Such strong local turbulent shear generates the turbulent eddies that trap the crystallites and cause the collision among the crystallites, thus affecting the aggregation of the nuclei particles. This dynamic process can be interpreted by using the Stokes number, defined by

$$St_\eta = \frac{\tau_p}{\tau_f} \tag{6.12}$$

where τ_p is the particle dynamic response time, and τ_f can be interpreted as the characteristic time of the locally generated turbulent eddies. τ_p and τ_f can be estimated by the following Equation (6.13)

$$\tau_p = \frac{\rho_p d_p^2}{18\mu}; \quad \tau_f = \sqrt{\frac{\nu}{\varepsilon}} \tag{6.13}$$

$$St_\eta = \frac{\rho_p}{18\mu\rho_L}\left(\frac{d_p}{\eta}\right)^2 \tag{6.14}$$

where ρ_p and ρ_L are the particle density and the solution density, respectively, and d_p is the particle size. η is the Kolmogorov turbulent eddy scale. Normally, if St_η <1, it indicates that particles will be trapped by the turbulent eddies, thus increasing the possibility of particle aggregation due to the collision so as to promote the growth of particle size, but will be also be confined by the eddy induced shear. It should be noted here that $\sqrt{\frac{\nu}{\varepsilon}}$ is the typical turn-over time of the locally generated turbulent eddies due to the turbulence induced shear.

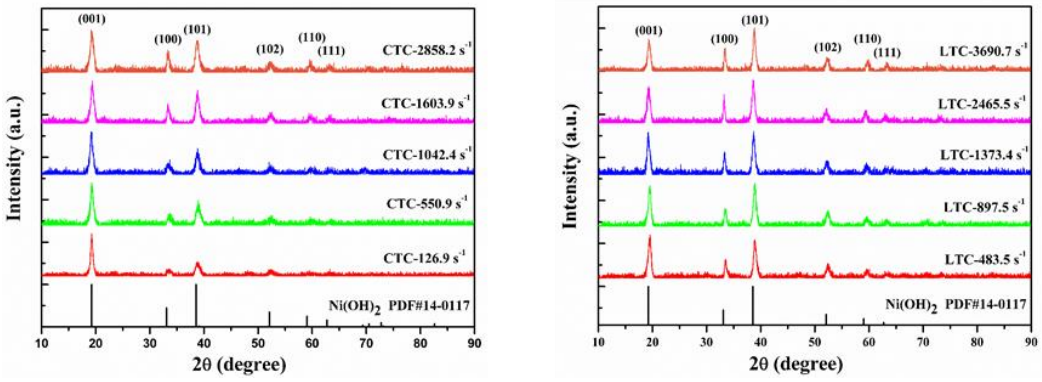

(a) (b)

Figure 6.4 XRD results of crystallite at different shear rates in the: (a) CTC; and (b) LTC.

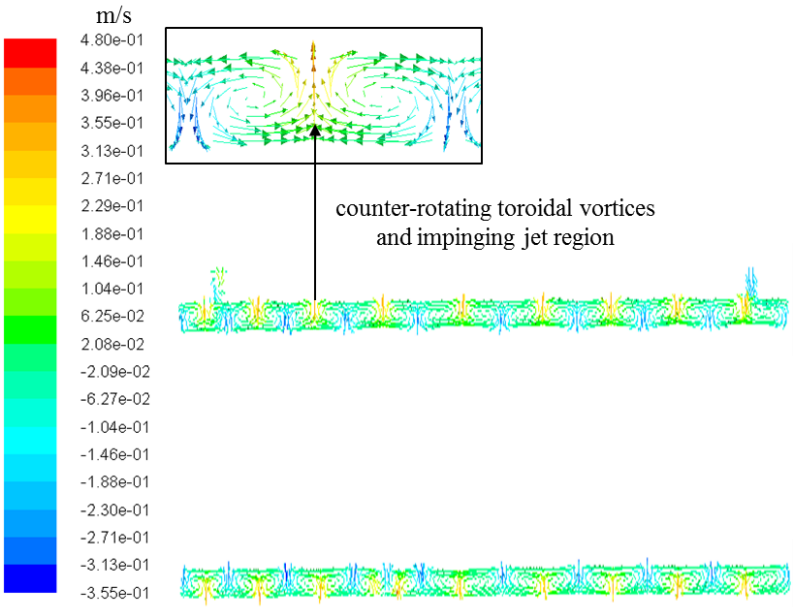

Figure 6.5 Radial velocity distribution in the vertical cutting plane of the CTC.

In order to calculate particle Stokes number of individual crystallites, the average crystallite size should be obtained first, which is estimated by the Scherrer equation

$$D = \frac{K\lambda}{\delta cos\theta} \tag{6.15}$$

where K is the shape factor, equal to 0.89 for NCM622 particles, λ is the wavelength of X-ray radiation, equal to 0.145056 nm, δ is the peak width at half minimum height, and θ is the diffraction angle. The crystallite size was calculated at different processing time from 1 to 8 hours, and the value ranges from 12 nm to 23.6 nm. Thus, there is little difference in crystallite size, which indicates that a single crystallite is hardly changed with processing time. Furthermore, the crystallite Stokes number was calculated with the order of 10^{-}

^{7}, which is much smaller than 1.0. This indicates that primary particles are closely transported and trapped by turbulent eddies. SEM images indicates that at the initial several hours, primary particles were loosely packed, forming aggregates. With an extension of the processing time, a long-term effect of entrapment leads to the agglomeration among these aggregates. Aggregates are stacked closely and bonded strongly. It has been observed from Figure 6.3 that the secondary particles at the processing time of 8 hours get more compact. Additionally, due to the long-time exposure to the local turbulent eddy induced shear, the surface of secondary particles becomes smooth, and the shape looks regular and spherical-like.

We also tested particle size and its distribution, as shown in Figures 6.6 (a) and 6.6 (b). The average particle size is small initially and increases until reaching a maximum, followed by a decreasing average size until levelling off. This trend is consistent with the formation mechanism of secondary particles. As the irregular and loosely packed aggregates are formed at first, there is not much reactant accumulating locally. However, with more reactants engulfed and trapped in eddies, the micro gaps among the aggregates are fully filled, and the local turbulent shear acting on the surfaces of these aggregates to shear off those of micro irregularity so as to yield regular shapes. It has been suggested by Ying *et al.* (2001) and Ying *et al.* (2004) that among various morphologies, the spherical one is the most effective in terms of packing density, as it has a rather small contact interface, which can lead to the least potential for bridge formation between particles. While the tap density of LiNCM622 cathode materials are generally dependent on the tap density of NCM622 precursors, it can be hypothesised that a high tap density may be beneficial for high electrical performance in terms of long life cycling (Liang *et al.*, 2014). Figure 6.6 (b)

illustrates the particle size distribution obtained at different processing times. The uniform distribution from the start of the particle formation suggests that the advantage of using the TC reactor for co-precipitation of micro particles is that it can provide relatively uniform turbulent shear distribution in the reaction chamber.

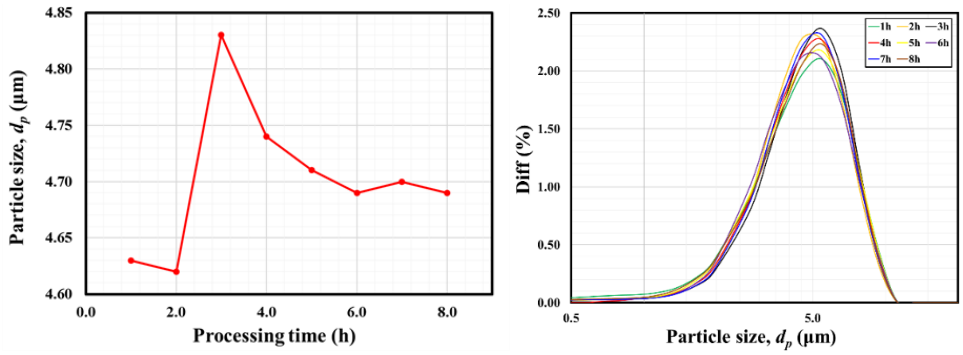

(a) (b)

Figure 6.6 (a) Particle size of NCM622 at different processing times in the CTC; and (b) Particle size distribution.

Some of the previous studies have indicated that the final NCM622 particles are secondary particles, assembled by a large number of nano-scaled primary particles (Thai *et al.*, 2015; Mayra and Kim, 2015; and Zhu *et al.*, 2019). By carefully observing the results of particle morphology and size from Figures 6.3 (a) and 6.6, it is suggested that the particles with a regular shape and a critical size can be obtained after the processing time exceeds 7 hours. Therefore, for the co-precipitation system of NCM622 precursor synthesis using the TC reactor in this study, the co-precipitation deems to reach the steady state after 7 hours, which is much shorter than that of using the traditional mixing tank reactor or continuous stirred tank reactor (CSTR). Considering this, the

experimental validation and analysis have taken the processing time to be 8 hours.

6.4.2 Effect of the cross-section profiles of inner cylinder and the mean shear rate

As the type of the rotational inner cylinder affects the Taylor vortices formed and the local turbulent shear flow behaviour, a lobed inner cylinder was also employed in the present study for assessing the effect of the cross-section profiles of inner cylinder on particles. The cross-sectional profile of this lobed geometry is composed of three arcs with the identical radian of 120°, connected by three mutual tangential lines. Investigations of the two geometries were conducted at different mean shear rates by the adoption of different rotational speeds. We employ the mean shear rate to characterise the effect of the turbulence induced shear instead of the rotational speed, as the mean shear rate is the overall effort contributed from the inner cylinder rotation, the gap size (affecting the volume for co-precipitation) and the type of the inner cylinder. The average mean shear rate in the TC reactor can be calculated by the following equation (Serra *et al.*, 1997),

$$\bar{G} = \sqrt{\frac{\bar{\varepsilon}}{\nu}} \tag{6.16}$$

The average turbulent dissipation rate $\bar{\varepsilon}$ was obtained from CFD simulation.

Table 6.3 summarises the values of shear rate, and corresponding primary particle size. It can be seen that the size of primary particles has little difference,

ranging from 12 nm to 23.6 nm. We also estimated the Kolmogorov length scale by Equation (6.17).

$$\eta = (\frac{\nu^3}{\varepsilon})^{1/4} \tag{6.17}$$

Apparently, the Kolmogorov length scale has the order of 10^{-5} m, which is much larger than the size of primary particles. Therefore, turbulent eddy shear has a very weak effect on crystallisation. Primary particles were only trapped, and then entrained by eddies. The comparison of length scale can also be found in Kim *et al.*'s (2011) study. However, their study only pointed out that fluid shear can act on particle size, but failed to interpret the interaction mechanism between them with different orders of length scale.

Table 6.3 Summary of flow field parameters and primary particle size at different rotational speeds.

Rotational speed $\boldsymbol{\Omega}$ (rpm)	Reynolds number *Re*		Shear rate G (s^{-1})		Kolmogorov length scale η ($\times 10^{-5}$ m)		Primary particle size D (nm)	
	CTC	LTC	CTC	LTC	CTC	LTC	CTC	LTC
300	3728	3837	126.9	483.5	14.67	7.51	14.5	15.1
500	6213	6396	550.9	897.5	7.04	5.52	23.6	19.9
700	8698	8954	1042.4	1373.4	5.12	4.46	14.5	13.7
1100	13668	14071	1603.9	2465.5	4.13	3.33	17.1	18.6
1500	18638	19188	2858.2	3690.7	3.09	2.72	12.0	16.4

The effects of the inner cylinder types and the corresponding shear rates on the crystal structure of the primary particles are illustrated in Figure 6.4. First of all, typical planes of (001), (100), (101), and (102) are shown in the XRD pattern. In addition, for the same inner cylinder cross-sectional profile, the appearance of characteristic diffraction peaks is almost not affected by adopting different mean shear rates for both the CTC and LTC. However, it is found that the peak intensity of planes (100) and (101) for the LTC increases with the increase of the mean shear rate greater than that for the CTC, indicating an improved crystallinity of primary particles. Such a growth preference were also observed in the works of Kim *et al.* (2011); Yang *et al.* (2016) and Wei *et al.* (2010). Crystal growth along plane (100) will show a good electrochemical performance, as plane (100) can provide proper paths for the fast transportation of lithium ion as suggested in these studies. Moreover, the relative peak intensity of plane (001) to plane (101) is different for the CTC and LTC. In the CTC, the crystal growth is mainly along plane (001), while in the LTC, the growth of plane (101) is faster than plane (001). This result also indicates the orientation of crystal growth under the influence of the local turbulent shear field.

The comparison of secondary particles in terms of the tap density, morphology, size and porosity has also been carried out at different mean shear rates for the CTC and LTC. Figure 6.3 (b) shows the evaluation of particle morphology with processing time in the LTC at the same rotational speed as the CTC. It is obvious that at the initial several hours, particles fail to be assembled with a regular shape in both the reactors. However, after 5 hours, the synthesized particles in the LTC present advantages in terms of spherical morphology, uniform size, and compact agglomeration. Figure 6.7 shows the change of particle size with

the increase of mean shear rate. The experimental validation was conducted by changing the rotational speed of the inner cylinder. For the same rotational speed, the mean shear rate in the LTC is greater than that in the CTC. For the CTC, the average particle size continuously decreases to 4 μm. In contrast, for the LTC, the particle size increases at smaller mean shear rate but gradually decreases to 6 μm. Furthermore, particle size synthesised in the LTC is greater than that synthesised in the CTC for the whole range of mean shear rates. Changes of the Kolmogorov length scale are also shown in Figure 6.7, where the Kolmogorov scale is calculated based on Equation (6.17). It can be seen from Figure 6.7 that the estimated Kolmogorov length scale is slightly greater than the particle size but they have the same order of magnitude. It should be noted here that the difference between the secondary particle size and the estimated Kolmogorov length scale is smaller for the LTC than that for the CTC. This finding indicates that the secondary particles may not only be well entrained by the turbulent eddies, but are still exposed to the turbulent eddy induced shear. By carefully inspecting the SEM results shown in Figure 6.8, it can be observed that the shape of NCM622 particles is regular with a spherical-like and smoother surface when increasing the mean shear rate. This effect is consolidated when using the LTC. In addition, Figure 6.9 shows the increased tap density of the NCM622 particles with the increase of shear rate. For the LTC, a high tap density of 2.25 g/cm^3 was reached at the shear rate of 3690.7 s^{-1}, which is larger than previously reported values (Thai *et al*., 2015; and Liang *et al*., 2014). Generally, the regular spherical particles can be compactly accumulated, which is beneficial for long life cycling (Liang *et al*., 2014).

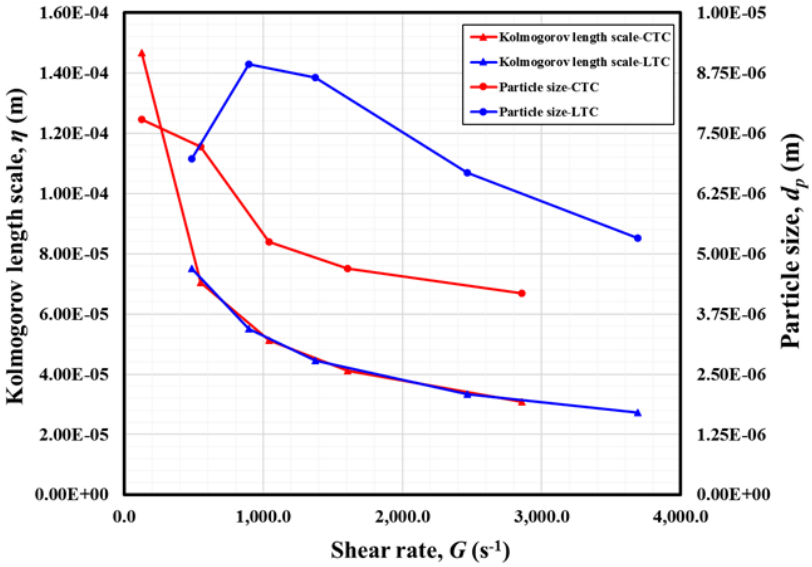

Figure 6.7 Particle size and Kolmogorov length scale at different shear rates.

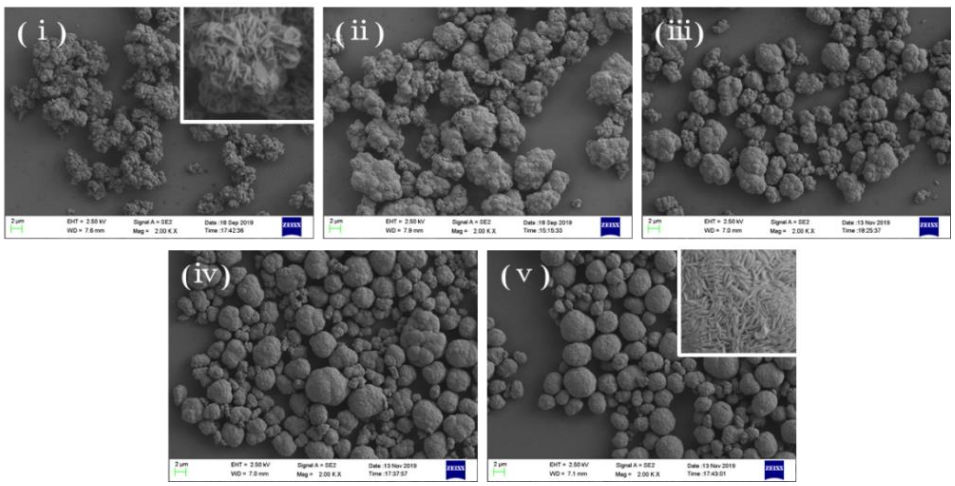

(a)

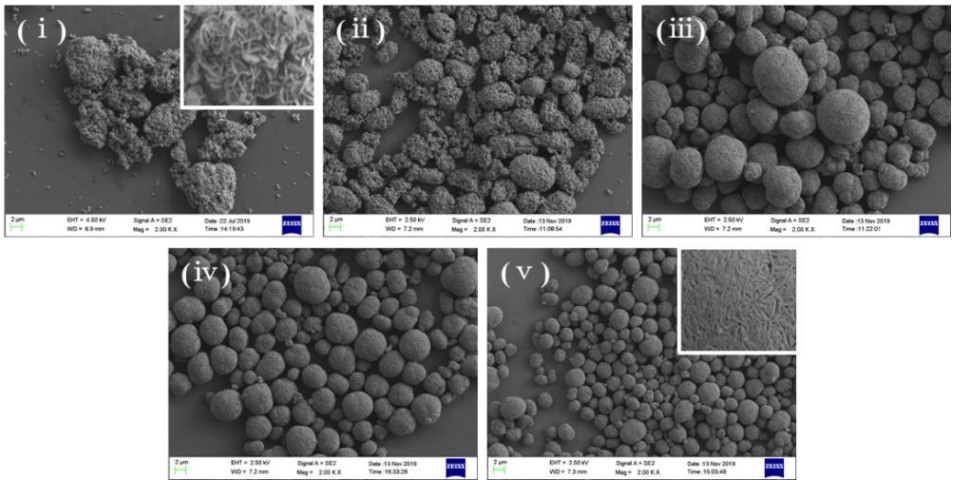

(b)

Figure 6.8 SEM images of NCM622 at different shear rates for the (a) CTC: (i) 126.9 s^{-1}; (ii) 550.9 s^{-1}; (iii) 1042.4 s^{-1}; (iv) 1603.9 s^{-1}; (v) 2858.2 s^{-1}; and (b) LTC: (i) 483.5 s^{-1}; (ii) 897.5 s^{-1}; (iii) 1373.4 s^{-1}; (iv) 2465.5 s^{-1}; (v) 3690.7 s^{-1}.

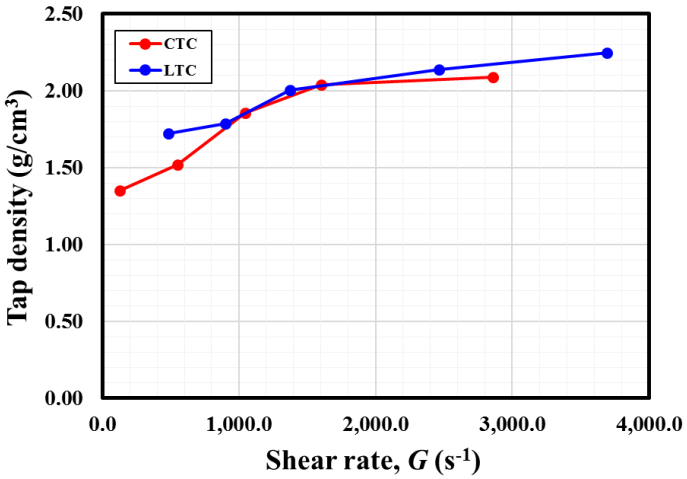

Figure 6.9 Tap density at different shear rates for the CTC and LTC.

The N_2 adsorption and desorption isotherm, and specific surface area of NCM622 particles are illustrated in Figures 6.10 (a), (b) and (c). The high porosity reflects more pores existing in the internal structure of particles. When

a large number of primary particles aggregate to form the secondary particle, pores will be generated in its internal while a loosely aggregated and packed structure leads to a high porosity. At smaller shear rates, aggregates fail to be combined compactly. Consequently, high porosity results from the loosely assembled aggregates. With increasing the shear rate, more primary particles entrapped by eddies can fill up the gaps among aggregates, developing into a rather regular shape. This result can be evidenced by examining the SEM images from the local amplification of those secondary particles as shown in Figure 6.10. It is obvious that with the increase of shear rate, particles are assembled compactly from the structure out-appearance, especially in the case of the LTC.

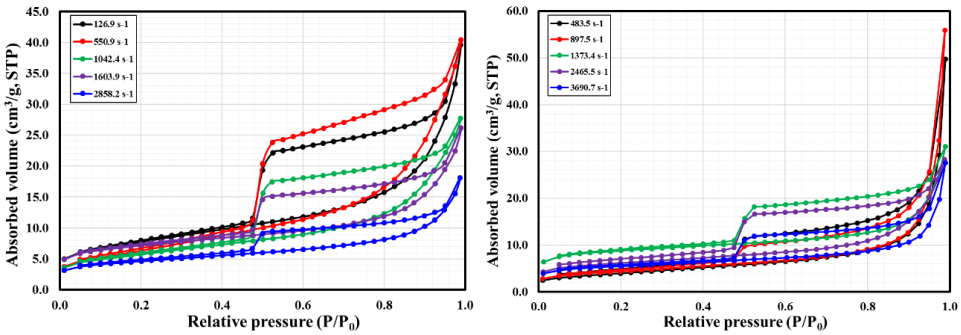

(a) (b)

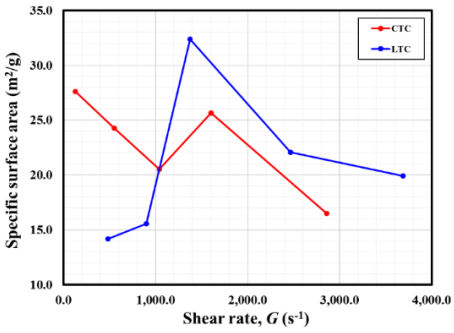

(c)

Figure 6.10 N_2 adsorption/desorption isotherm at different shear rates in the: (a) CTC; and (b) LTC; (c) Specific surface area at different shear rates.

The above results and discussion have shown the existence of strong correlation between the synthesised particle properties and the turbulent eddy shear rate. It can be deduced that the local turbulent shear controls both primary and secondary particle growth and collision, assembly and agglomeration of aggregates. The turbulent eddy induced shear force can act on the surface of secondary particles as shown schematically in Figure 6.11. According to Sung *et al.*'s (2000) study, the size of yttrium oxalate agglomerates increases with the increase of agitation speed until 700 rpm, suggesting that if turbulent shear is not enough to overcome the interactive force between agglomerates, particles will keep continuous growth. In Thai *et al.*'s (2015) study, they found that when the rotational speed of TC crystallizer exceeds 300 rpm, shear force will be stronger than interactive force. Our study has shown that the synthesised particle properties are strongly affected by the turbulent eddy shear rate that correlates with the rotational speed and the cross-sectional profiles of inner cylinder of the TC reactor.

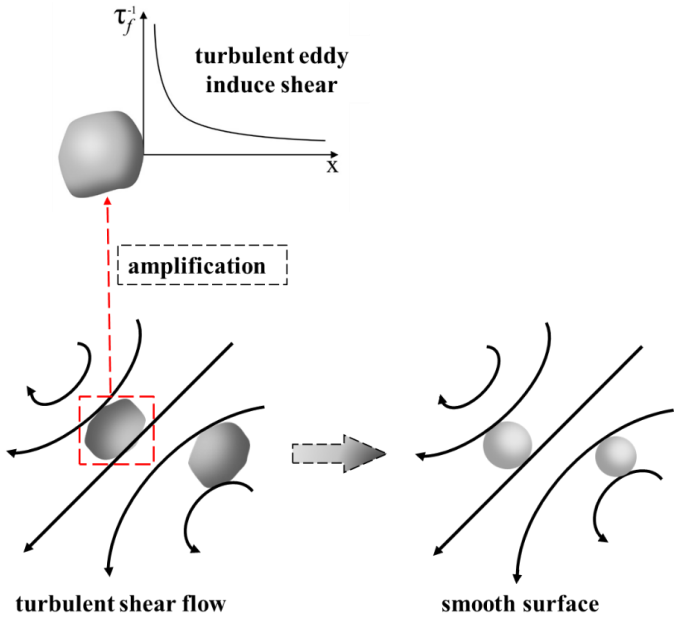

Figure 6.11 Schematic representation of particles in a turbulent shear flow.

Figure 6.12 shows the time averaged velocity field and shear strain rate in the CTC and LTC. Both cases take three rotational speeds, 500 rpm, 1100 rpm, and 1500 rpm, respectively, for comparisons. It can be seen from the figure that both the mean velocity and the shear strain rate in the impinging jet regions formed in the vicinity of the inner cylinder surface between the two Taylor vortices are strengthened with the increase of the mean shear rate. As the velocity gradient increases, the entrapment effect due to the local turbulent shear is enhanced. This effect becomes remarkable, especially for the LTC, as the lobed inner cylinder generates the periodic variation of gap size. Gap area is critical for the identification of flow pattern, and the impinging jet flows also occurs in such an area. Firstly, it can be seen from Equation (6.1) that Reynolds number which is used to determine global turbulence degree, depends on the gap size. For the constant gap size in the CTC, turbulent condition can be hardly changed significantly once the rotational speed is given. However, for the LTC, the gap

size becomes temporal-periodic, which keeps changing with the rotation of the inner cylinder, and this variation may generate the local flow separation behind the top of lobed inner cylinder so as to induce more turbulent eddies locally. In this case, the formation and the deformation of Taylor vortex always exist, thus Taylor vortex with a constant size cannot be created, Accordingly, more turbulent eddies can be induced compared to the CTC. These eddies will further interact with particles. On one hand, eddy entrapment contributes to the compactness of agglomerates. On the other hand, small eddies down to the Kolmogorov scale are generally recognised to be isotropic. This indicates an evenly distributed eddy shear acting on particle surface, which will eventually result in the formation of particles with regular shape. Secondly, as can be seen from Figure 6.12 (a) that the jet velocity is enhanced in the large gap area when employing the LTC. Due to the relative high velocity of jet flows impinging to the wall, more turbulent eddies will be created, thus the local turbulent shear is enhanced. Therefore, the aforementioned factors in the gap area may contribute to the formation of desired particle properties in the LTC.

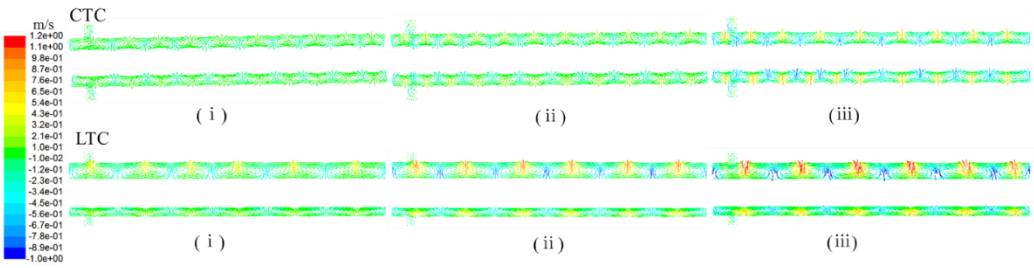

(a)

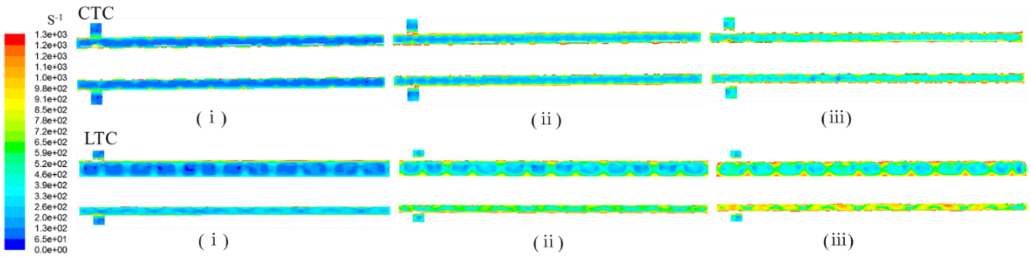

(b)

Figure 6.2 (a) Radial velocity distributions; and (b) Shear strain rate distribution at different inner cylinder rotational speeds: (i) 500 rpm; (ii) 1100 rpm; and (iii) 1500 rpm.

6.4.3 Micromixing

As can be seen from the previous discussion, hydrodynamic micromixing plays an important role in the co-precipitation process in the TC reactor, which has a significant impact on the synthesized particle properties. Generally speaking, fast mixing can result in the high local supersaturation, which will further facilitate nucleation process. The increase of nucleation rate is beneficial to the creation of a large number of primary particles, thus leading to a small particle size. To this end, particle size may be seen as an indicator of the degree of mixing at all the scales, including macro level to molecular level.

Figure 6.13 shows the values of the variations of the mean mixture fraction $\bar{\xi}$ with time in the middle cylindrical surface of the gap. By definition, $\bar{\xi}$ ranges from 0.0 to 1.0, and the value of 0.5 is deemed to achieve a perfect macro-mixing, thus giving out a homogenously completed mixing. In our CFD modelling, $\bar{\xi}$ was assumed to 0.0 at the inlet of MSO_4 solution, and 1.0 at the inlet of NaOH solution. It can be seen from the figure that the mixing condition

is poor inside the reactor at the onset of reactants injection. A value of $\bar{\xi}$ far from 0.5 often indicates a non-homogeneous environment. This could be the reason for the appearance of irregular particle morphology at the first several hours of the co-precipitation synthesis, observed from the SEM images. The value of $\bar{\xi}$ gradually approaches 0.5 with time, indicating an effective mixing to be achieved. It is interesting to note that the time to attain a relatively good mixing required for the LTC is shorter than that for the CTC. This clearly indicates a relatively fast formation of well-established macro-mixing condition in the LTC. Furthermore, high mean shear rate can also improve the mixing at macro scale. As can be seen from the figure, the time for setting-up of the macro mixing becomes shorter with the increase of the mean turbulent shear rate, but this difference disappears when the rotational speed of the inner cylinder is greater than 1100 rpm.

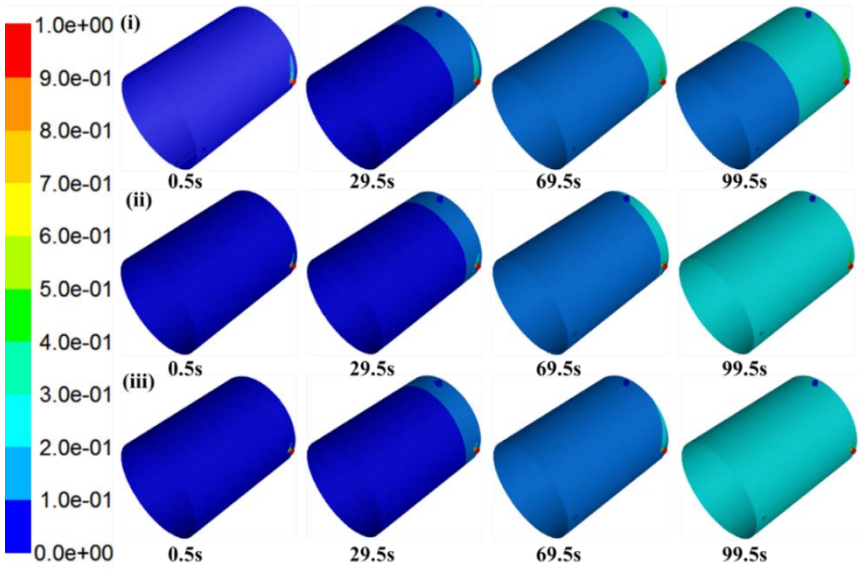

(a)

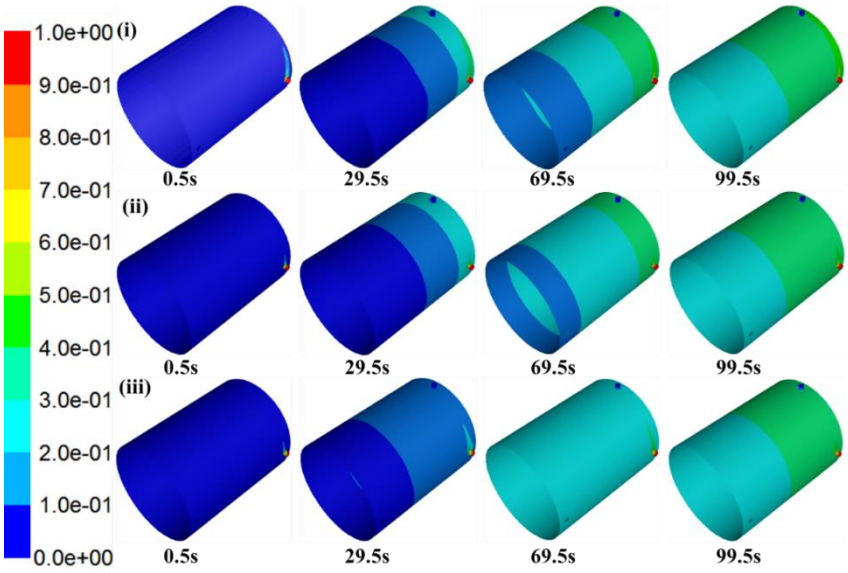

(b)

Figure 6.33 Mean mixture fraction $\bar{\xi}$ in the middle cylindrical surface of the gap for the: (a) CTC; and (b) LTC at different inner cylinder rotational speeds: (i) 500 rpm; (ii) 1100 rpm; and (iii) 1500 rpm.

Since the co-precipitation chemical reaction occurs at molecular level, the other variable for characterisation of the micromixing, the mixture fraction variance $\overline{\xi'^2}$ is used here to estimate the degree of micromixing. Figure 6.14 illustrates the distribution of the variance ratio ($\overline{\xi'^2}/\overline{\xi'^2}_{max}$) along the circumferential direction in the vertical cutting plane. Such distribution is used to characterise the micromixing performance due to geometrical modification. It can be seen that high values of $\overline{\xi'^2}$ mainly concentrate in the inlet regions, which decrease with the rotation of the inner cylinder. The mixing process can be described as follows. After reactants are introduced into the system, large-scale variance is generated, but smoothed out by the turbulent diffusion with small-scale variance to be dissipated by molecular diffusion. Turbulent eddy shear facilitates the mixing process, thus creating a uniform environment and small variance. To

effectively describe such micromixing behaviour, a correlation coefficient between $\overline{\xi'^2}$ and the cross-sectional average turbulent energy dissipation rate $\bar{\varepsilon}$ in the circumferential direction for the given axial position of the reactor is introduced as defined by

$$R = \frac{\overline{\xi'^2}(\theta)\cdot\bar{\varepsilon}(\theta)}{\sqrt{\overline{\xi'^2}^2(\theta)}\cdot\sqrt{\overline{\bar{\varepsilon}^2(\theta)}}} \tag{6.18}$$

Figure 6.15 shows the results of correlation coefficient *R* in the circumferential direction around the inner cylinder. Such correlation may be used to forecast the position of good micromixing so that the cross-sectional profiles of inner cylinder can be altered accordingly. It is revealed from Figure 6.15 that more peaks of *R* are observed in the CTC than those in the LTC when using the same rotational speed. However, the non-zero value of $\overline{\xi'^2}$ often indicates poor micromixing. The large value of *R* suggests a greater local turbulent energy dissipation and poor micromixing environment. By comparing Figures 6.15 (a) and (b), it can be clearly observed that the number of peaks of *R* is reduced for the case of using the lobed inner cylinder, indicating that the micromixing occurring in the LTC is better than that in the CTC. This implies that the micromixing behaviour can be improved through the alteration of the cross-sectional profiles of inner cylinder for the TC reactor.

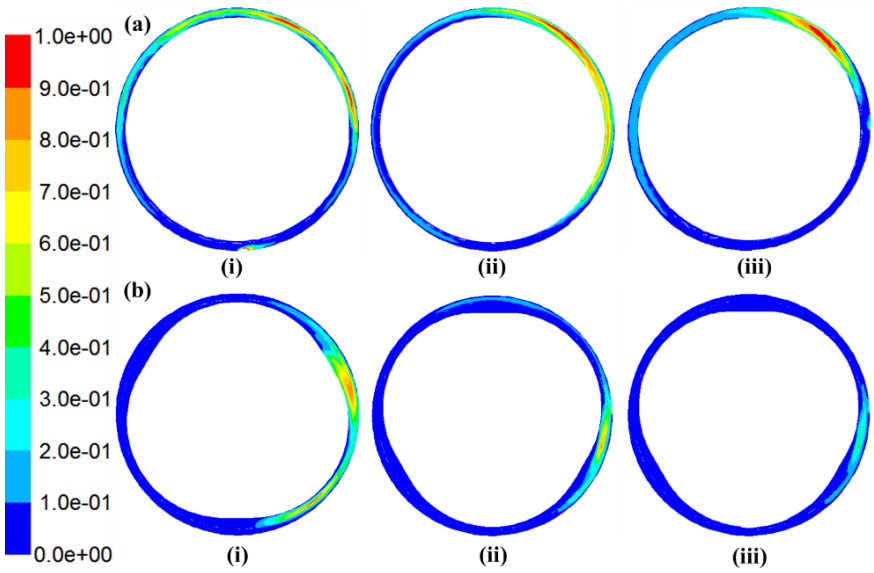

Figure 6.4 Distribution of the ratio of mixture fraction variance ($\overline{\xi'^2}/\overline{\xi'^2}_{max}$) for the: (a) CTC; and (b) LTC at different inner cylinder rotational speeds: (i) 500 rpm; (ii) 1100 rpm; and (iii) 1500 rpm.

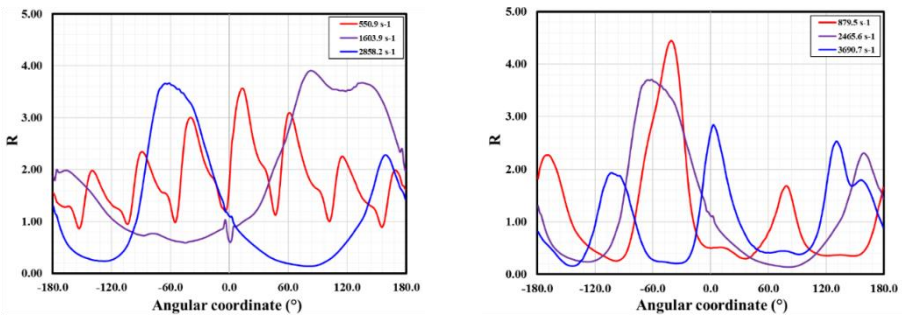

(a) (b)

Figure 6.5 Spatial correlation between mixture fraction variance and turbulent energy dissipation rate for the: (a) CTC; and (b) LTC.

6.5 Conclusions

Modelling of co-precipitation synthesis of NCM622 precursor for cathode material of lithium ion batteries in the TC reactor with classical circular and lobed inner cylinder profiles has been carried out by CFD simulation and experimental validations. The effects of processing time, inner cylinder type and the turbulent mean shear rate on the co-precipitation synthesis of micro-particles were investigated. The main conclusions reached from the present study are as follows:

(1) The employment of the TC reactor for synthesis of micro-particles can significantly reduce the processing time. In particular, the impinging jet region created in the middle of a pair of counter-rotating toroidal vortices increases the turbulent shear gradient, thus the shear rate.

(2) The local turbulent shear imposed to the synthesised suspension particles can either increase the size of particles or inhibit the growth of particles. For those particles whose size is much smaller than the Kolmogorov length scale, turbulent eddies can enhance the entrapped particle collision, thus resulting in more particles aggregation to form large size particles. However, once the shear force caused by the turbulent eddy exerting on agglomerates exceeds the internal bonding force among the agglomerates, the size of agglomerated particles will be suppressed. Also, the periodic variation of gap size for lobed inner cylinder in the LTC is beneficial to the generation of increased velocity gradient in the impinging jet regions, yielding a strong local turbulent energy dissipation rate.

(3) The mixing behaviour of reactants (MSO_4 solution and NaOH solution) was assessed using CFD modelling. It is revealed from the simulation that the mean

mixture fraction $\bar{\xi}$ representing the mixing degree at macro scale can take a shorter time to reach the required mixing condition for NCM622 co-precipitation synthesis at a higher shear rate, especially for the LTC. The micro scale mixing, characterised by the mixture fraction variance $\overline{\xi'^2}$, the key indicator to evaluate local supersaturation for molecular reaction, has a strong correlation with the turbulent energy dissipation rate. This correlation can be used for the evaluation of the micromixing performance, which may assist the selection of different cross-sectional profiles of the inner cylinder in the TC reactor for co-precipitation synthesis of micro-particles with better properties.

References

Bensaid, S., Deorsola, F.A., Marchisio, D.L., Russo, N. and Fino, D., 2014. Flow field simulation and mixing efficiency assessment of the multi-inlet vortex mixer for molybdenum sulfide nanoparticle precipitation. *Chemical Engineering Journal*, *238*, pp.66-77.

Cao, H., Zhang, Y., Zhang, J. and Xia, B., 2005. Synthesis and electrochemical characteristics of layered $LiNi_{0.6}Co_{0.2}Mn_{0.2}O_2$ cathode material for lithium ion batteries. *Solid State Ionics*, *176*(13-14), pp.1207-1211.

Casanova, H. and Higuita, L.P., 2011. Synthesis of calcium carbonate nanoparticles by reactive precipitation using a high pressure jet homogenizer. *Chemical Engineering Journal*, *175*, pp.569-578.

Ceder, G. and Mishra, S.K., 1999. The Stability of Orthorhombic and Monoclinic-Layered LiMnO2. *Electrochemical and Solid State Letters*, *2*(11), p.550.

Chen, X., Jia, X., Qu, Y., Chen, D. and Chen, Y., 2018. High-voltage performance of concentration-gradient $Li[Ni_{0.6}Co_{0.2}Mn_{0.2}]O_2$ layered oxide cathode materials for lithium batteries. *New Journal of Chemistry*, *42*(8), pp.5868-5874.

Cheng, K.L., Mu, D.B., Wu, B.R., Wang, L., Jiang, Y. and Wang, R., 2017. Electrochemical performance of a nickel-rich $LiNi_{0.6}Co_{0.2}Mn_{0.2}O_2$ cathode material for lithium-ion batteries under different cut-off voltages. *International Journal of Minerals, Metallurgy, and Materials*, *24*(3), pp.342-351.

Cui, Y., Liu, K., Man, J., Cui, J., Zhang, H., Zhao, W. and Sun, J., 2019. Preparation of ultra-stable $Li[Ni_{0.6}Co_{0.2}Mn_{0.2}]O_2$ cathode material with a

continuous hydroxide co-precipitation method. *Journal of Alloys and Compounds*, *793*, pp.77-85.

Duan, X., Feng, X., Yang, C. and Mao, Z.S., 2016. Numerical simulation of micro-mixing in stirred reactors using the engulfment model coupled with CFD. *Chemical Engineering Science*, *140*, pp.179-188.

Fox, R.O., 2003. *Computational Models for Turbulent Reacting Flows*. Cambridge university press.

Gan, C., Hu, X., Zhan, H. and Zhou, Y., 2005. Synthesis and characterization of $Li_{1.2}Ni_{0.6}Co_{0.2}Mn_{0.2}O_{2+\delta}$ as a cathode material for secondary lithium batteries. *Solid State Ionics*, *176*(7-8), pp.687-692.

Gradl, J., Schwarzer, H.C., Schwertfirm, F., Manhart, M. and Peukert, W., 2006. Precipitation of nanoparticles in a T-mixer: coupling the particle population dynamics with hydrodynamics through direct numerical simulation. *Chemical Engineering and Processing: Process Intensification*, *45*(10), pp.908-916.

Grossmann, S., Lohse, D. and Sun, C., 2016. High–reynolds number taylor-couette turbulence. *Annual Review of Fluid Mechanics*, *48*, pp.53-80.

He, P., Yu, H. and Zhou, H., 2012. Layered lithium transition metal oxide cathodes towards high energy lithium-ion batteries. *Journal of Materials Chemistry*, *22*(9), pp.3680-3695.

Kim, M.H., Shin, H.S., Shin, D. and Sun, Y.K., 2006. Synthesis and electrochemical properties of Li $[Ni_{0.8}Co_{0.1}Mn_{0.1}]O_2$ and Li $[Ni_{0.8}Co_{0.2}]O_2$ via co-precipitation. *Journal of Power Sources*, *159*(2), pp.1328-1333.

Kim, J.M., Chang, S.M., Chang, J.H. and Kim, W.S., 2011. Agglomeration of nickel/cobalt/manganese hydroxide crystals in Couette–Taylor crystallizer. *Colloids and Surfaces A: Physicochemical and Engineering Aspects*, *384*(1-3), pp.31-39.

Kweon, H.J., Kim, S.J. and Park, D.G., 2000. Modification of LixNi1− yCoyO2 by applying a surface coating of MgO. *Journal of Power Sources*, *88*(2), pp.255-261.

Lathrop, D.P., Fineberg, J. and Swinney, H.L., 1992. Transition to shear-driven turbulence in Couette-Taylor flow. *Physical Review A*, *46*(10), pp.6390-6405.

Lee, M.H., Kang, Y.J., Myung, S.T. and Sun, Y.K., 2004. Synthetic optimization of $Li[Ni_{1/3}Co_{1/3}Mn_{1/3}]O_2$ via co-precipitation. *Electrochimica Acta*, *50*(4), pp.939-948.

Lee, S.W., Kim, H., Kim, M.S., Youn, H.C., Kang, K., Cho, B.W., Roh, K.C. and Kim, K.B., 2016. Improved electrochemical performance of $LiNi_{0.6}Co_{0.2}Mn_{0.2}O_2$ cathode material synthesized by citric acid assisted sol-gel method for lithium ion batteries. *Journal of Power Sources*, *315*, pp.261-268.

Li, G., Yang, X. and Ye, H., 2015. CFD simulation of shear flow and mixing in a Taylor–Couette reactor with variable cross-section inner cylinders. *Powder Technology*, *280*, pp.53-66.

Liang, L., Du, K., Peng, Z., Cao, Y., Duan, J., Jiang, J. and Hu, G., 2014. Co-precipitation synthesis of $Ni_{0.6}Co_{0.2}Mn_{0.2}(OH)_2$ precursor and characterization of $LiNi_{0.6}Co_{0.2}Mn_{0.2}O_2$ cathode material for secondary lithium batteries. *Electrochimica Acta*, *130*, pp.82-89.

Liu, Y. and Fox, R.O., 2006. CFD predictions for chemical processing in a confined impinging-jets reactor. *AIChE Journal*, *52*(2), pp.731-744.

Liu, L., Yang, X., Li, G., Huang, X. and Xue, C., 2020. Shear controllable synthesis of barium sulfate particles using lobed inner cylinder Taylor-Couette flow reactor. *Advanced Powder Technology*, 31(3), pp.1088-1099.

Marchisio, D.L., Rivautella, L. and Barresi, A.A., 2006. Design and scale-up of chemical reactors for nanoparticle precipitation. *AIChE Journal*, *52*(5), pp.1877-1887.

Mayra, Q.P. and Kim, W.S., 2015. Agglomeration of Ni-Rich hydroxide in reaction crystallization: Effect of Taylor vortex dimension and intensity. *Crystal Growth & Design*, *15*(4), pp.1726-1734.

Morales, J., Perez-Vicente, C. and Tirado, J.L., 1990. Cation distribution and chemical deintercalation of $Li_{1-x}Ni_{1+x}O_2$. *Materials Research Bulletin*, *25*(5), pp.623-630.

Ren, D., Shen, Y., Yang, Y., Shen, L., Levin, B.D., Yu, Y., Muller, D.A. and Abruña, H.D., 2017. Systematic optimization of battery materials: key parameter optimization for the scalable synthesis of uniform, high-energy, and high stability $LiNi_{0.6}Mn_{0.2}Co_{0.2}O_2$ cathode material for lithium-ion batteries. *ACS Applied Materials & Interfaces*, *9*(41), pp.35811-35819.

Serra, T., Colomer, J. and Casamitjana, X., 1997. Aggregation and breakup of particles in a shear flow. *Journal of Colloid and Interface Science*, *187*(2), pp.466-473.

Sun, Z., Jiao, L., Fan, Y., Li, F., Wang, D., Han, D. and Niu, L., 2016. Industrialization of tailoring spherical cathode material towards high-capacity, cycling-stable and superior low temperature performance for lithium-ion batteries. *RSC Advances*, *6*(100), pp.97818-97824.

Sung, M.H., Choi, I.S., Kim, J.S. and Kim, W.S., 2000. Agglomeration of yttrium oxalate particles produced by reaction precipitation in semi-batch reactor. *Chemical Engineering Science*, *55*(12), pp.2173-2184.

Thai, D.K., Mayra, Q.P. and Kim, W.S., 2015. Agglomeration of ni-rich hydroxide crystals in taylor vortex flow. *Powder Technology*, *274*, pp.5-13.

Wei, G.Z., Lu, X., Ke, F.S., Huang, L., Li, J.T., Wang, Z.X., Zhou, Z.Y. and Sun, S.G., 2010. Crystal habit-tuned nanoplate material of $Li[_{Li1/3–2x/3}Ni_xMn_{2/3–x/3}]O_2$ for high-rate performance lithium-ion batteries. *Advanced Materials*, *22*(39), pp.4364-4367.

Xu, L., Zhou, F., Kong, J., Chen, Z. and Chen, K., 2018. Synthesis of $LiNi_{0.6}Mn_{0.2}Co_{0.2}O_2$ with sodium DL-lactate as an eco-friendly chelating agent and its electrochemical performances for lithium-ion batteries. *Ionics*, *24*(8), pp.2261-2273.

Yakhot, V., Orszag, S.A., Thangam, S., Gatski, T.B., Speziale, C.G., 1992. Development turbulence models for shear flow by a double expansion technique. *Physics of Fluids A: Fluid Dynamics*, *4*(7), pp.1510-1520.

Yang, C.K., Qi, L.Y., Zuo, Z., Wang, R.N., Ye, M., Lu, J. and Zhou, H.H., 2016. Insights into the inner structure of high-nickel agglomerate as high-performance lithium-ion cathodes. *Journal of Power Sources*, *331*, pp.487-494.

Ying, J., Wan, C., Jiang, C. and Li, Y., 2001. Preparation and characterization of high-density spherical $LiNi_{0.8}Co_{0.2}O_2$ cathode material for lithium secondary batteries. *Journal of Power Sources*, *99*(1-2), pp.78-84.

Ying, J., Jiang, C. and Wan, C., 2004. Preparation and characterization of high-density spherical $LiCoO_2$ cathode material for lithium ion batteries. *Journal of Power Sources*, *129*(2), pp.264-269.

Yuan, J., Wen, J., Zhang, J., Chen, D. and Zhang, D., 2017. Influence of calcination atmosphere on structure and electrochemical behavior of $LiNi_{0.6}Mn_{0.2}Co_{0.2}O_2$ cathode material for lithium-ion batteries. *Electrochimica Acta*, *230*, pp.116-122.

Yue, P., Wang, Z., Peng, W., Li, L., Chen, W., Guo, H. and Li, X., 2011. Spray-drying synthesized $LiNi_{0.6}Mn_{0.2}Co_{0.2}O_2$ and its electrochemical

performance as cathode materials for lithium ion batteries. *Powder Technology*, *214*(3), pp.279-282.

Zhu, Q., Xiao, H., Zhang, R., Geng, S. and Huang, Q., 2019. Effect of impeller type on preparing spherical and dense $Ni_{1-x-y}Co_xMn_y(OH)_2$ precursor via continuous co-precipitation in pilot scale: A case of $Ni_{0.6}Mn_{0.2}Co_{0.2}(OH)_2$. *Electrochimica Acta*, *318*, pp.1-13.

CHAPTER 7

CONCLUSIONS AND RECOMMENDATIONS

7.1 Hydrodynamically controllable synthesis of fine particles

The aim of this PhD work is to investigate the effects of the key hydrodynamic parameters on particle formation process in order to realize the controllable synthesis of fine particles by using various TC reactors. As a fundamental case study, barium sulfate was chosen as a model substance. The experimental parameter study of the preparation process of barium sulfate particles has been conducted, focusing on the initial supersaturation, reactant feeding rate, inner cylinder rotational speed (characterized by Reynolds number $Re = \frac{\omega d r_i}{\nu}$). The formation of fine aggregates based on crystallites, particle morphology, size and size distribution have been carefully observed in these designed experiments and the results obtained have been analysed. CFD modelling was also employed to assist the acquirement of the hydrodynamics such as shear induced turbulent energy dissipation rate, turbulent kinetic energy distribution and particle-eddy interactions occurring in the reactor, coupled with Lagrangian particle tracking to obtain the particle dispersion in the synthesis process. As an extension, the same modelling approach was also applied to the other reactive synthesis system, the preparation of NCM622 particles, an important precursor material for lithium ion batteries. The mixing of reactants in the TC reactor was comprehensively investigated. As the outcomes of the present studies, the main accomplishments of this project can be summarised as:

(1) Three different kinds of morphology of barium sulfate particles (i.e., flake, transition and granule) were produced by reactive precipitation in the LTC. The influence of the operating conditions, including the rotational speed of the inner cylinder, reactant feeding rate and initial supersaturation on the morphology transition have been examined. An empirical equation was proposed involving shear rate (rotational speed) and feeding rate. Such equation can be served as an indicator for morphology transition.

(2) The comparison of hydrodynamic characteristics between the CTC and LTC in terms of barium sulfate particle size, size distribution, and turbulence induced shear has indicated that the adoption of the LTC is effective to realise shear controllable synthesis of the particles with the desired properties due to the intensification of the turbulence eddy induced shear. A strong correlation between the synthesized particle size and the local turbulent dissipation rate has been identified.

(3) The experiments on the evaluation of micromixing efficiency in the TC reactor have been performed by using a parallel competing iodide-iodate reaction system. A relative small value of *Xs* under all tested conditions in the LTC suggests a good micromixing performance. This result is in an agreement with the CFD modelling result in terms of turbulent intensity. Micromixing time calculated according to the incorporation model is found to be the order of 10^{-5} s, much smaller than that of the conventional stirred tank reactor (2×10^{-3} to 2×10^{-2} s).

(4) A large number of barium sulfate particles were tracked using Euler-Lagrange approach with consideration of the interfacial forces acting on the

particles. It has been revealed that the particle trajectories in both the CTC and LTC exhibit the behaviour of helical movement, being entrapped and strongly affected by Taylor vortices. Such interaction has reaffirmed the effect of turbulent shear in such reactors on the particle synthesis process, i.e. the control of particle properties due to the local turbulent eddies induced shear. Particle radial distribution indicates that there exists a separation strap of the particles inside and outside the vortices due to the different particle axial velocity, which can be used for particle classification. Particle axial dispersion coefficient presents a similar distribution curve to the particle size distribution, and the dispersion coefficient for the LTC is greater than that for the CLC. These results indicate more effective global mixing in the LTC than that in the CTC due to the enhanced deformation of Taylor vortices at the gap region of the LTC.

(5) The LTC was also successfully applied to the other reactive synthesis system, the preparation of NCM622 particles. Both CFD simulation and experiments were used for validation of the hydrodynamic characteristics of the synthesis process. The synthesized particle properties in terms of particle size, morphology and specific surface area by using the LTC are also found to be remarkably improved in comparison to the use of the CTC. This may be attributed to the enhanced shear rate in the impinging jet regions formed in the vicinity of the lobed inner cylinder surface for the LTC. Evaluation of the mixing between reactants has been made by implementing two user-defined scalars, $\bar{\xi}$ and $\overline{\xi'^2}$, revealing that better macromixing and micromixing can be more quickly obtained in the LTC than the CTC.

The specific realisations of the aforementioned claims are described in the following section.

7.2 Specific realizations

7.2.1 Synthesis of barium sulfate particles

The synthesis of the model substance, barium sulfate was firstly realised in the TC reactor (both the CTC and LTC). Both particle morphology and particle size have been assessed and studied in detail as reported in Chapters 2 and 3, respectively. The key parameters investigated include initial supersaturation, feeding rate, inner cylinder rotational speed (characterized by Reynolds number or shear rate). In Chapter 2, the interfacial phenomena in terms of particle morphology transition was studied in detail for the synthesis using the LTC. According to the SEM results, three different kinds of morphology are observed to take place, the outer-appearance of the shapes being classified as flake, transition and granule. It has been found that particle morphology transition is strongly dependent on the transition of flow patterns inside the LTC. At low concertation, particle morphology transition is observed to occur at the onset of turbulent Taylor-Couette flow, however, such morphology transition also appears at the onset of turbulent Taylor vortex flow at high concentration. It should be noted that the classification of flow patterns is based on Reynolds number $Re = \frac{\omega d r_i}{\nu}$, which can be changed by adjusting the rotational speed of the inner cylinder. It is also found that the formed particles exist in the form of agglomerate rather than single individual crystals. Both micromixing of reactants and mass transfer from bulk solution to the surface of the particle determine the final particle morphology. Subsequently, the mechanism of particle formation in such TC system has been proposed through examining the results by looking into the combined effects of both the rotational speed and feeding rate. An empirical correlating equation is thus presented for the

application of the cases of low initial supersaturation, yielding the quantitative description about the particle morphology. At a high supersaturation, it is found that particles are favourable to form granules due to the enhanced nucleation rate.

Starting from Chapter 2, a series of explorations to identify the TC reactor as a promising device for reactive precipitation of fine particles were conducted. In order to demonstrate the proposed LTC to have better performance than that of the traditional CTC, comparisons on the final products by using both reactors were also made. Thus, in Chapter 3, particle size and particle size distribution affected by hydrodynamic characteristics when using different types of inner cylinders under various operating conditions were particularly investigated. To reveal the impact of the hydrodynamics of Taylor-Couette flow due to the variation of the inner cylinder on the particles, CFD modelling was adopted. Before simulation, flow domain in the TC reactor was constructed by Design Modeller while the computational mesh was created by using ICEM, a mesh generation code embedded in ANSYS software. A sliding mesh method was adopted in the vicinity of the inner cylinder to circumvent the effect of irregular cross-section profile of the lobed geometry when the inner cylinder is rotating. The numerical calculation on hydrodynamics in the TC reactor was conducted by using FLUENT 17.0 as the experimental visualisations and observation on the particle synthesis in the TC reactor are still forbidden, especially for particle aggregation and the local turbulent eddies. Based on the results of SEM, XRD and simulated turbulence time and length scales, it is found that turbulent eddies may have little effect on crystallite formation process, but they may determine the final particle (or agglomerate) size and the size distribution as the turbulent eddies with the length scale down to the Kolmogorov scale will impose a strong

shear on the particle surface. It has been demonstrated that particle size is smaller, and the size distribution is narrower in the LTC with the increase of the inner cylinder rotational speed than those in the CTC. It should be noted here that the only difference between the CTC and LTC lies in the cross-sectional profile of the inner cylinder. The change in the inner cylinder cross-sectional profiles leads to the intensification of the impinging jet flows between the Taylor vortices in the LTC, which are formed between two typical counter-rotating Taylor vortices. As a result, the velocity gradient in the radial direction increases, and the local turbulent shear is enhanced. A correlation between the synthesized particle size and the local turbulent dissipation rate (shear rate is a function of dissipation rate) was given with the change of sampling time to demonstrate the dependence of particle size on turbulent eddy induced shear. Sampling time can serve as a reference to indicate an appropriate time during particle preparation.

From the perspective of the preparation of barium sulfate particles, it is revealed that compared with the CTC, the use of the LTC can effectively improve the process of reactive precipitation through changing the turbulence induced shear strain rate distribution in the inwards and outwards impinging jet regions of Taylor vortices, which is beneficial to the formation of small particles with regular morphology and narrow size distribution. Turbulence generated not only has effects on final particles by exerting shear force on particle surface, but also determines the environment for chemical reaction. As chemical reaction takes place at the molecular level, mixing at the similar scale can directly influence its course. That means micromixing creates supersaturation, subsequently inducing chemical reaction. In order to quantitatively demonstrate the difference of the micromixing performance for the CTC and LTC, the trial

reaction by employing the Villermaux iodide-iodate reaction system has been performed and the results are reported in Chapter 4. Several factors were examined by carefully collecting samples while the determination of sample collection time has been done in such a way to ensure the reliable UV results in principle. The acid concentration was also carefully chosen to avoid over-loading, while the injection of acid was controlled to keep the feeding as slow as possible to eliminate the impact of the macromixing in the TC reactor. Comparing the value of segregation index, *Xs*, it is suggested that the hydrodynamic heterogeneity created by the LTC can significantly enhance micromixing efficiency. Moreover, the characteristic micromixing time, estimated by the incorporation model was calculated. Four ordinary differential equations were solved by the forth-order Runge-Kutta iteration. It is found that the micromixing time in the TC reactor is about three orders of magnitude lower than that of the conventional stirred tank reactor. Thus, when considering the enhancement of micromixing performance, alteration of the configuration of the inner cylinder would be an effective way for intensification of the process of particle preparation.

As a Taylor vortex and its typical structure determine the local hydrodynamic environment for particle formation, the dynamic interaction between Taylor vortices and the particles was studied in Chapter 5. In order to observe such interaction, barium sulfate particle trajectories based on the input for the simulation specified according to the actual properties of experimentally synthesized particles were tracked using Euler-Lagrange approach. Considering the TC reactor to be vertically installed, the buoyancy, drag and lift forces were considered to be dominant in the particle movement and thus implemented into the simulation. Also, in order to include the effect of turbulence on particle

dispersion, stochastic tracking model was employed. By observing particle trajectories in the TC reactor, particle motion exhibits a helical movement, entrapped by Taylor vortices. Particles with high velocity magnitude tend to distribute in the large gap regions in the LTC, likely being attributed to the entrainment of particles by the impinging jet flows towards these regions, and the periodic gradually decrease gap for the LTC, where the flow in circumferential experiences an expansion following by a contraction. Particle or particle dispersion is significantly enhanced by increasing the inner cylinder rotational speed, and changing inner cylinder type from the CTC to LTC. In particular, velocity gradient in radial direction can bring out particle classification due to the difference in particle axial velocity. Particle axial dispersion can be seen as an indicator to characterise the global mixing. With the increase of the rotational speed, less time is needed for the particles to disperse a certain axial distance. Also, the calculated axial diffusion coefficient shows a similar distribution curve to the particle size distribution, and such coefficient for the LTC is greater and distribution is more even than those for the CLC, indicating that the local shear strain rate is enhanced due to the inner cylinder cross-sectional profile modification and more turbulent eddies are generated due to the periodic variation of gap size in the LTC. The results of particle tracking are consistent with the deduction as indicated in Chapter 3 that the utilisation of the LTC can effectively intensify the process of particle preparation.

7.2.2 Synthesis of NCM622 particles

Further study by employing the TC reactor was carried out both experimentally and numerically on the reactive system of co-precipitation of NCM622 particles.

As described in Chapter 6, the effects of processing time, inner cylinder type and the turbulent mean shear rate on particle preparation have been assessed and discussed. Processing time should be identified firstly, as this will provide the time scale for the products to reach a steady state. It is found that by employing the TC reactor, the processing time can be significantly reduced to 8 hours, which is much shorter than that by using the conventional stirred tank reactor with an estimation of at least 60 hours. For the comparison of inner cylinder types (i.e., CTC and LTC), the synthesised particle characteristics at various mean shear rates was characterized based on particle size, morphology and specific surface area. The diffraction peak intensity from the XRD measurement indicates the orientation of crystal growth under the influence of the local turbulent shear, where the peak intensity of planes (100) and (101) increases with the increase of the mean shear rate for the LTC. As for the change of particle size, particle size in the LTC is greater than that in the CTC. This difference may be attributed to the different turbulence induced shear features, which is characterised by Kolmogorov length scale turbulent eddies as the particles will interact with such turbulent eddies. For those particles with the size much smaller than the Kolmogorov length scale, turbulent eddies can enhance the entrapped particle collision, thus resulting in more particles aggregation to form large size particles. However, once the shear force caused by the turbulent eddy exerting on agglomerates exceeds the internal bonding force among the agglomerates, the size of agglomerated particles will be suppressed. Such effect becomes apparent in the LTC due to its periodic variation of gap size of the lobed inner cylinder.

Different from Chapter 4, which has evaluated the micromixing performance of the TC reactor, the mixing of the reactants assessed by two variables was carried

out in Chapter 6. The calculation of these two variables was implemented into the simulation by using UDS. Comparison was focused on the mean shear rate generated by the rotation of the inner cylinder in the CTC and LTC. It is revealed that the mixture fraction, $\bar{\xi}$, representing the mixing degree at macro sales, can take a shorter time to reach the required mixing condition for co-precipitation synthesis at a higher shear rate, especially for the LTC. The micro scale mixing, characterised by mixture faction variance, $\overline{\xi'^2}$ the key indicator to evaluate local supersaturation for molecular reaction, has a strong correlation with the turbulent energy dissipation rate. Such correlation can be seen as an indicator for the selection of different cross-sectional profiles of the inner cylinder in the TC reactor in order to obtain desired product characteristics.

7.3 Recommendations for future work

This PhD work has concentrated on one key issue, the effects of fluid dynamics on the course of fine particle preparation in the TC reactor by means of reactive precipitation, focusing on shear controllable synthesis of fine particles. Barium sulfate was chosen as a model particle to carry out the fundamental study. Then, the co-precipitation of NCM622 particles was also successfully achieved by using the TC reactor. The results obtained from particle quality, micromixing performance and hydrodynamics simulation, together with the particle-turbulent eddy interaction can be used as a guidance for process intensification by means of the optimization of the reactor configuration, or the development of novel reactors. Although hydrodynamics has been explored in this project, there are still remaining many problems that need to be addressed in understanding the nature and the effects of the hydrodynamic heterogeneity

encountered in the TC reactor. Based on the accomplishment of present work, some recommendations for future work are summarised as follows:

(1) The flow field was simulated with the Reynolds Average Navier-Stokes (RANS) equations coupled with RNG k-ε turbulence model in current work. This means flow field information is presented with the mean value. However, chemical reaction coupled with mass transfer is dependent on the mixing at a micro scale which is generally smaller than the grid size. Also, the local turbulence structures still have not been resolved sufficiently by using such simulation approach, as eddies are assumed to be isotropic. In order to further understand and distinguish the inherent structures of turbulent eddies, large eddy simulation (LES) is suggested to be adopted as large eddies are resolved directly while isotropic small eddies can be modelled. Consequently, mixing can be better described at even small scale. However, LES requires finer meshes than those for RANS calculation and a long flow-time is needed to obtain the stable statistics, thus the computational cost is acceptably high. These shortcomings can be circumvented by improving the simulation capability.

(2) As for the simulation of particle trajectories, barium sulfate was treated as the spherical particle. The numerical simulation conducted is to realize the quantitative measurement of the particle dispersion on the effect of Taylor vortices embedded by small turbulent eddies. It has been recognised that the drag force experienced by the particles plays a leading role in determining the particle trajectories for the liquid-solid system especially when the density of the particles is much greater than that of the liquid. This is true in the present particle synthesis process. However, the assumption of spherical particle will bring certain deviation from the reality, especially for the case of the synthesised

particles that present various shapes. For conducting more rigorous simulations, variation of the particle shapes should be taken into consideration. For an irregular shape of particle, shear stress and static pressure exerting on the particle surface are not evenly distributed, thereby the surface integral on these force contributions will give out different result comparing with a smooth surface spherical particle. For simplification, the final particle size distribution obtained from the experimental observations can be reasonably used at the onset of particle injection from the inlet, served as the boundary condition for the simulation of particle dispersion in the TC reactor. However, further work on the correction of the drag law equation and particle size changing with time is suggested to be realised in the numerical simulation of the particle dispersion, which can be achieved by adopting the user-define function (UDF) in ANSYS Fluent code.

(3) It has been denoted in Chapter 6, final cathode material, LiNCM622 can inherit the morphology and structure from NCM622 precursor. Only NCM622 particles have been concerned in this PhD work. The experimental work is the first step in understanding the mechanism of turbulent eddy-particle interaction. Subsequent studies including calcination, characterization of electrochemical performance, and surface modification are still necessary for the establishment of a complete system of the cathode material formation. Also, for a theoretical investigation, simulation based on molecular behaviour is strongly suggested, which enables the visualization of working mode of the lithium ion batteries, such as lithium ion diffusion, phase transition of crystal growth, and temperature distribution.

(4) For a multi-phase reactive system, the interaction between liquid and solid has been involved in this work. However, there are still some inadequacies which need to be circumvented, so that the reactive precipitation coupling with hydrodynamic effect on the course of fine particle preparation can be fully captured. For example, chemical reaction with detailed kinetics is suggested to be involved into the simulation, which can be realised by solving species transport, where the species can be defined as the reactant concentration or the relevant parameter which is closely related to the mass transfer in the synthesis of the fine particles. Moreover, the effect of turbulent eddies on particle agglomeration is another important factor during crystallization, which is suggested to be considered in the simulation. This process can be realised by using the population balance model (PBM) by taking agglomeration kinetics, collision caused by turbulent eddy motion and Brownian motion into consideration. In order to validate such effect, modelling results can be further compared and corrected according to the current experimental results of particle size distribution. Although such reactive precipitation system is complicated and challengeable to be simulated due to the complicated coupling of many parameters and high computational cost, it would be much beneficial to implement chemical reaction kinetics into the current two-phase modelling, which will provide the physical insight into the effects of hydrodynamics on the overall process of reactive precipitation, thereby completely modelling the sophisticated controllable synthesis system.

LIST OF PUBLICATIONS

Journal articles

Liu, L., Yang, X., Li, G., Huang, X. and Xue, C., 2020. Shear controllable synthesis of barium sulfate particles using lobed inner cylinder Taylor-Couette flow reactor. *Advanced Powder Technology, 31*(3), pp.1088-1099.

Guo, Y., Yang, X., Li, G., Yang, J., **Liu, L.**, Chen, L., and Li, B., 2021. Shear Turbulence Controllable Synthesis of Aggregated Nano-Particles Using a Swirling Vortex Flow Reactor Assisted by Ultrasound Irradiation. *Chemical Engineering Journal*, 405, 126914.

Major revision

Liu, L., Yang, X., Yang, J., Li, G., and Guo, Y., 2020. Modelling of turbulent shear controllable coprecipitation synthesis of lithium ion battery cathode precursor micro-particles in a Taylor-Couette flow reactor with variable configurations of inner cylinder. (submitted to *Chemical Engineering Journal*).

Liu, L., Yang, X., Yang, J., Li, G., and Guo, Y., 2020. Effect of hydrodynamic heterogeneity on micromixing intensification in a Taylor-Couette flow reactor with variable configurations of inner cylinder. (submitted to *AIChE Journal*).

Under review

Liu, L., Yang, X., Yang, J., Li, G., and Guo, Y., 2020. Effect of hydrodynamic heterogeneity on particle aggregate dispersion in a Taylor-Couette flow reactor with variable configurations of inner cylinder. (submitted to *Powder Technology*).

Book chapter

Liu, L., Li, G., Yang, X., Huang, X. and Xue, C., 2019. Interfacial Phenomena in the Synthesis Process of Barium Sulfate Particles Precipitated in a Lobed Inner Cylinder Taylor-Couette Flow Reactor: Effects of Fluid Dynamics. In *Wettability and Interfacial Phenomena-Implications for Material Processing*. IntechOpen.